CZECH TECHNICAL UNIVERSITY
IN PRAGUE

Faculty of Nuclear Sciences and Physical Engineering

Department of Physics

Research project

Measurement of incoherent J/ψ photoproduction in Pb-Pb collisions with ALICE

Author: Bc. David Grund
Supervisor: prof. Jesús Guillermo Contreras Nuño, Ph.D.
Academic year: 2019/2020

ČESKÉ VYSOKÉ UČENÍ TECHNICKÉ
V PRAZE

Fakulta jaderná a fyzikálně inženýrská

Katedra fyziky

Výzkumný úkol

Měření nekoherentní J/ψ fotoprodukce v Pb-Pb srážkách na ALICE

Autor: Bc. David Grund
Školitel: prof. Jesús Guillermo Contreras Nuño, Ph.D.
Akademický rok: 2019/2020

Prohlášení

Prohlašuji, že jsem svůj výzkumný úkol vypracoval samostatně a použil jsem pouze podklady (literaturu, projekty, software, atd.) uvedené v přiloženém seznamu.

Nemám závažný důvod proti použití tohoto školního díla ve smyslu § 60 Zákona č. 121/2000 Sb., o právu autorském, o právech souvisejících s právem autorským a o změně některých zákonů (autorský zákon).

V Praze dne ....

....

David Grund

Acknowledgments

I would like to express my sincere gratitude to my supervisor prof. Jesús Guillermo Contreras Nuño, Ph.D. for all fruitful discussions, invaluable advices, language corrections and continuous effort when guiding my work and writing of the thesis. Also, I would like to thank Mgr. Michal Broz, Ph.D. for the preparation of nanoAOD data sets which were used as an input to the presented analysis.

David Grund

Title:
Measurement of incoherent J/ψ photoproduction in Pb-Pb collisions with ALICE

Author: David Grund

Specialisation: Experimental Nuclear and Particle Physics

Sort of project: Research project

Supervisor: prof. Jesús Guillermo Contreras Nuño, Ph.D., Department of Physics, Faculty of Nuclear Sciences and Physical Engineering, Czech Technical University in Prague

Consultant: —

Abstract: The photoproduction of vector mesons, such as J/ψ, is one of the processes that can occur in ultra-peripheral collisions (UPCs) at hadronic accelerators. Apart from the coherent production of vector mesons, cross section of which can be directly related to the parton distribution functions describing the quark and gluon content of hadrons, the incoherent photoproduction shows to be sensitive to fluctuations in the number of partons and their position in the transverse plane. Research in such processes can thus shed light on the fundamental aspects of the high-energy QCD physics, example of which is the phenomenon of gluon saturation.

The first steps of the analysis of the incoherent J/ψ photoproduction in Pb-Pb UPCs at the LHC with the ALICE detector are presented. The increase in luminosity offers a substantial increase in the number of midrapidity incoherent events produced at $\sqrt{s_{\mathrm{NN}}} = 5.02$ TeV compared to the previous ALICE measurement at $\sqrt{s_{\mathrm{NN}}} = 2.76$ TeV. This could substantially reduce statistical uncertainties as well as help us to understand better potential systematic effects.

Key words: ALICE, ultra-peripheral collisions, photoproduction of J/ψ, energy-dependent hot-spot model

Název práce:
Měření nekoherentní J/ψ fotoprodukce v Pb-Pb srážkách na ALICE

Autor: David Grund

Obor: Experimentální jaderná a částicová fyzika

Druh práce: Výzkumný úkol

Vedoucí práce: prof. Jesús Guillermo Contreras Nuño, Ph.D., Katedra fyziky, Fakulta jaderná a fyzikálně inženýrská, České vysoké učení technické v Praze

Konzultant: —

Abstrakt: Fotoprodukce vektorových mezonů, například J/ψ, je jedním z procesů, ke kterým může docházet při ultra-periferálních srážkách na hadronových urychlovačích. Kromě koherentní produkce, jejíž účinný průřez přímo souvisí s tvarem partonových distribučních funkcí popisujících kvarkové a gluonové složení hadronů, je významným procesem také nekoherentní fotoprodukce citlivá na fluktuace počtu partonů a jejich pozic v příčné rovině. Výzkum těchto procesů může přinést důležité poznatky při studiu fundamentálních jevů kvantové chromodynamiky při vysokých energiích, jejichž příkladem je gluonová saturace.

Ve výzkumném úkolu jsou představeny první kroky analýzy nekoherentní fotoprodukce J/ψ mezonů v Pb-Pb srážkách na LHC naměřených detektorem ALICE. Navýšení luminosity umožňuje analyzovat výrazně vyšší počet nekoherentně vyprodukovaných mezonů v centrální oblasti rapidity při těžišťové energii srážky $\sqrt{s_{\mathrm{NN}}} = 5.02$ TeV ve srovnání s původními výsledky ALICE změřenými při $\sqrt{s_{\mathrm{NN}}} = 2.76$ TeV. Toto by mohlo výrazně omezit statistické chyby měření, a umožnit tak lépe prozkoumat možné systematické nepřesnosti.

Klíčová slova: ALICE, ultra-periferální srážky, fotoprodukce J/ψ, energeticky závislý hot spot model

Contents

List of figures

List of tables

Introduction

Ultra-peripheral collisions are a powerful tool for examining the fundamental aspects of QED and especially of high-energy QCD physics and the structure of hadrons. At the LHC, when the distance between the colliding hadrons exceeds the sum of their radii, the interaction is photon-induced because possible hadronic interactions between the projectiles are suppressed to a minimum due to the short range of the strong force. These processes are called ultra-peripheral collisions (UPCs).

An important example of a process that can occur in heavy-ion UPCs is the photoproduction of a vector meson, such as ρ, J/ψ, ϕ and others. The coherent photoproduction is of particular interest as the cross section is sensitive to the shape of the parton distribution functions (PDFs) describing the quark and gluon content of hadrons. It was found that at high energies (low Bjorken x) the structure of hadrons evolves and cannot be interpreted as a cluster of valence quarks only, but is rather dominated by an increasing number of gluons and quark-antiquark pairs. However, it is expected that the number of gluons cannot rise to infinity. At a certain point, the energy evolution is believed to be tamed by the phenomenon of gluon saturation, which has not yet been observed experimentally.

On the other hand, when the photon interacts with only one nucleon in the nucleus, the process is referred to as the incoherent photoproduction. The importance of the incoherent cross section lies in its sensitivity to fluctuations both in the number of partons and in their positions in the transverse plane. Hence, the coherent and incoherent vector meson photoproduction in collisions of heavy ions constitute a valuable experimental instrument to improve our understanding of high-energy QCD physics.

This document is organised as follows. Chapter 1 is dedicated to the description of deeply inelastic scattering and the historical development of understanding the structure of hadrons. In addition to the original parton model and observed violations of the Bjorken scaling, later discoveries and gluon saturation are presented.

Ultra-peripheral collisions are classified and reviewed in Chapter 2. Here the QED part of the process concerning the emission of a quasireal photon and the photon flux as well as the QCD part comprising the interaction of the photon with the hadronic target are discussed. Several models of the latter process are introduced, including the important colour dipole model within which the photon is thought to fluctuate into a quark-antiquark pair.

Chapter 3 introduces a recently-presented energy-dependent hot-spot model used to describe the hadronic structure in ultra-peripheral collisions in terms of hot spots, the number of which grows when the energy of the collision increases. Two main papers are reviewed, dedicated to the application of the model to both γ-p and heavy-ion collisions.

The ALICE detector at the LHC is an example of an experimental accelerator facility where UPCs are studied extensively. The description of ALICE and its subdetector systems is presented in Chapter 4. A more detailed description is given only for the detectors that are necessary for the measurement of incoherent J/ψ production at midrapidity in UPCs.

The only existing analysis of the incoherent photoproduction of the J/ψ meson by ALICE, based on data from the Run 1 at the LHC, is presented in Chapter 5.

Eventually, Chapter 6 summarizes my contribution to the analysis of J/ψ photoproduction on the LHC data collected by ALICE in 2018 during the LHC Run 2. Firstly, the utilized data samples, triggers and selections of events are described, followed by the calculation of the integrated luminosity and signal extraction achieved through fits to the invariant mass distributions of the analysed samples.

Chapter 1

Structure of hadrons

1.1 Deeply inelastic scattering

This section loosely follows the lecture handouts on Deeply Inelastic Scattering by M. Thomson [1], Part 6 of the book [2], and is supplemented with some historical facts from the Nobel lecture by J. I. Friedman [3].

By the end of 1960s, the idea of using high-energy electrons as a probe to examine the internal structure of nucleons became feasible thanks to the development of particle accelerators. This kind of experiment is called deeply inelastic scattering (DIS) and, in general, it consists of a lepton (with a sufficiently small wavelength) scattering off a nucleon while the latter disintegrates. In 1990, J. I. Friedman, H. W. Kendall and R. E. Taylor from MIT and SLAC were awarded the Nobel Prize in Physics for their contribution to DIS experiments performed in the late 1960s on the 20 GeV Stanford linear accelerator completed in 1966. The outcome of these experiments served among others as an experimental evidence of the quark model.

Considering just the leading process, DIS can be understood as an exchange of one virtual electro weak gauge boson (γ, $W^{\pm}$ or Z^0). The Feynman diagram for the case of an electron-proton scattering via photon exchange is illustrated in Fig. 1.1.

In the rest of this section, just the laboratory frame (the rest frame of a target proton) and an electron as a probe will be considered. Let's denote the four-momenta of the participating particles in this frame as $k = (E_e, \boldsymbol{k})$ (incident electron), $k' = (E'_e, \boldsymbol{k'})$ (scattered electron), $p = (M_p, \boldsymbol{0})$ (proton), $q = (\nu, \boldsymbol{q})$ (virtual photon) and $w = (W, \boldsymbol{w})$ (hadronic state X). Then, $\nu = E_e - E'_e$ is equal to the energy loss of the incident electron. There exists a set of Lorentz invariant variables describing DIS:

- **Virtuality** of the exchanged photon $Q^2 = -q^2 = -(k - k')^2$, which is equal to squared momentum transfer from the primary electron to the proton.

- **Invariant mass** $W^2 = (p + q)^2 = M_p^2 + 2pq - Q^2 = M_p^2 + 2M_p\nu - Q^2$ of the final hadronic state X.

- **Bjorken variable** x defined as $x = \frac{Q^2}{2pq} = \frac{Q^2}{2M_p\nu}$. When considering elastic scattering, W^2 must be equal to M_p^2, which means that $2pq = Q^2$ (equivalent to saying $x = 1$). Thus in the case of DIS, $0 < x < 1$.

- **Inelasticity** $y = \frac{pq}{pk}$. In the rest frame of the proton the relation $y = \frac{\nu}{E_e}$ holds, giving y the

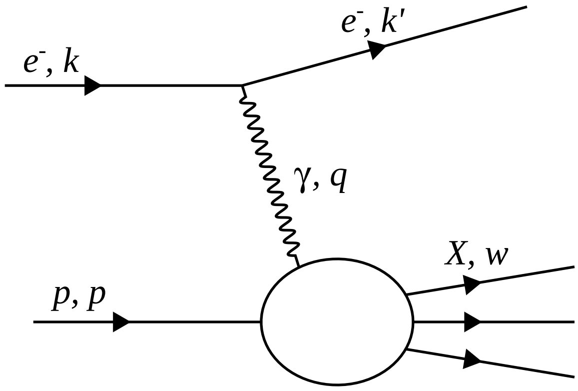

Figure 1.1: Sketch of deeply inelastic scattering between an electron and a proton. See text for the definition of the variables.

meaning of a ratio of energy loss to incident energy. Its value is 0 for elastic scattering and in range (0,1] for the inelastic case.

- **Mandelstam variable** $s = (k+p)^2$, which is equal to the invariant mass of the whole system.

A simple expression can be derived that relates the above defined variables with s, namely

$$Q^2 = xy(s - M_p^2) \quad \Leftrightarrow \quad x = \frac{Q^2}{y(s-M_p^2)}\,, \tag{1.1}$$

using which one can easily deduce that the collision with a higher total energy $\sqrt{s}$ corresponds to a lower value of the x-variable.

The DIS cross section at a fixed s can be expressed in terms of two independent variables from the set above, as opposed to elastic scattering, where a sole variable (typically the scattering angle θ) is sufficient to describe the final state. For the elastic electron-proton scattering, the differential cross section is known as the Rosenbluth formula

$$\begin{aligned}\frac{\mathrm{d}\sigma}{\mathrm{d}\Omega} &= \left(\frac{\mathrm{d}\sigma}{\mathrm{d}\Omega}\right)_{\text{Mott}} \frac{E'_e}{E_e}\left(\frac{G_E^2+\tau G_M^2}{1+\tau} + 2\tau G_M^2 \tan^2\frac{\theta}{2}\right) \\ &= \frac{\alpha^2}{4E_e^2\sin^4\frac{\theta}{2}}\frac{E'_e}{E_e}\left(\frac{G_E^2+\tau G_M^2}{1+\tau}\cos^2\frac{\theta}{2} + 2\tau G_M^2\sin^2\frac{\theta}{2}\right)\,,\end{aligned} \tag{1.2}$$

where α is the fine-structure constant, $\tau = \frac{Q^2}{4M_p^2}$, $G_E(Q^2)$ ($G_M(Q^2)$) is the electric (magnetic) form factor of the proton and $(\mathrm{d}\sigma/\mathrm{d}\Omega)_{\text{Mott}}$ is the Mott cross section describing the elastic scattering of a relativistic electron off a proton where the proton recoil is neglected.

Moving on to the inelastic case, one can give the differential cross section for example in terms of θ and E'_e (as these can be easily measured)

$$\frac{\mathrm{d}\sigma}{\mathrm{d}\Omega\mathrm{d}E'_e} = \frac{\alpha^2}{4E_e^2\sin^4\frac{\theta}{2}}\left(W_2\left(\nu,Q^2\right)\cos^2\frac{\theta}{2} + 2W_1\left(\nu,Q^2\right)\sin^2\frac{\theta}{2}\right)\,, \tag{1.3}$$

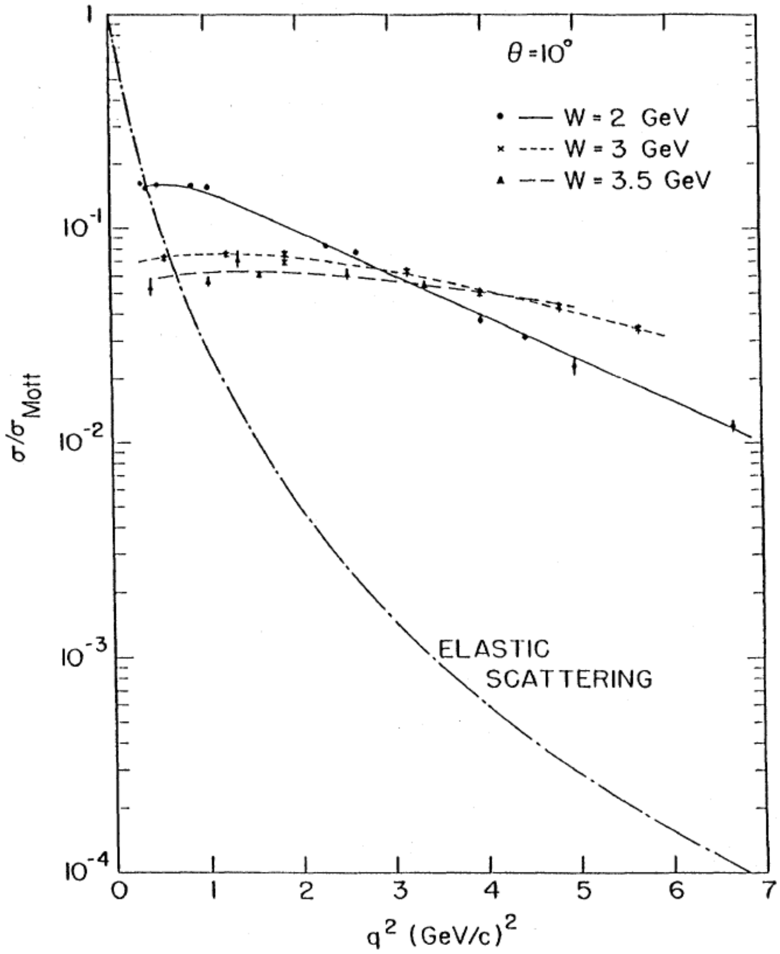

Figure 1.2: The ratios of the elastic and the inelastic differential cross sections to the Mott differential cross section and their dependence on q^2 [3]. The measurement was performed at the scattering angle $\theta = 10^\circ$ for three different invariant masses W.

which resembles the previous formula but the proton form factors are replaced with the proton structure functions $W_1(\nu,Q^2)$ and $W_2(\nu,Q^2)$. Values of these functions must be determined experimentally measuring the differential cross section at different values of the scattering angle θ and the energy of the scattered electron E_e. The early results appeared to be unexpected since the DIS cross section did not fall as rapidly with increasing q^2 as the elastic cross section ($\sim q^{-6}$) and showed rather weak q^2-dependence as illustrated in Fig. 1.2 for the scattering angle $\theta = 10^\circ$ and various invariant masses W.

Before going further, it is convenient to introduce dimensionless structure functions as

$$F_1(x,Q^2) = MW_1(\nu,Q^2)\,, \tag{1.4}$$
$$F_2(x,Q^2) = \nu W_2(\nu,Q^2)\,, \tag{1.5}$$

using which one can rewrite the cross section into the form that is often used,

$$\frac{\mathrm{d}^2\sigma}{\mathrm{d}x\mathrm{d}Q^2} = \frac{4\pi\alpha^2}{Q^4}\left[\left(1 - y - \frac{M_p x y}{s}\right)\frac{F_2(x,Q^2)}{x} + y^2 F_1(x,Q^2)\right]\,. \tag{1.6}$$

The second surprising behaviour which emerged from the experimental data is referred to as the *Bjorken scaling*, proposed by J. D. Bjorken in 1969. According to this concept, confirmed by

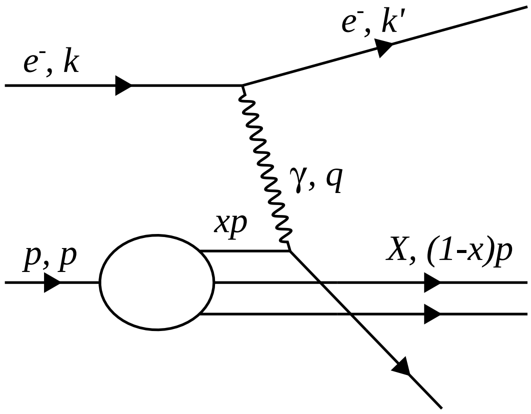

Figure 1.3: The parton model of DIS.

the early observations, the structure functions F_1 and F_2 should be almost constant functions of Q^2 at fixed x and should only *scale* with the dimensionless variable x. It thus suggests that the proton substructure is independent of the probe energy. This led R. Feynman in around 1969 to develop the so called *parton model* in which the proton is thought to be build up of point-like constituents – *partons*, but without specifying what the partons actually are.

Now, another physical meaning of the Bjorken variable becomes apparent. Assuming the simple parton model is valid, DIS can be interpreted as the *elastic* scattering of the electron on one of the partons. If $Q^2 \gg M_p^2$, one can show that x has the meaning of a fraction of the proton four-momentum p (or equivalently its three-momentum $\boldsymbol{p}$) that is carried by the struck parton (i.e. xp), see Fig. 1.3. The parton model only works in the "infinite momentum frame" of the proton where both the proton and the parton masses can be neglected as well as the transverse motion of the partons, so the proton is regarded as a stream of non-interacting (almost free) fast partons.

Nonetheless, it is worth mentioning here that a number of attempts employing different models describing the electron-proton interaction in DIS and models of the nucleon structure emerged to explain the observed data from the DIS experiments. These included several non-constituent models (such as Vector Meson Dominance) as well as constituent models treating the anticipated constituents of the proton (partons) in different manners. Besides the attempt to identify partons with quarks, which were proposed independently by M. Gell-Mann and G. Zweig in 1964 as an ordering scheme to classify hadrons, there was the approach of Drell, Levy and Yan to identify partons with bare nucleons and pions. After several years of ongoing experiments, enough data were gathered to claim the predictions based on the parton-quark identification had proven to be in the best accordance with the measurements. Some of these results will be presented in the rest of this section.

Assuming the parton-quark identification is justifiable, one can compare Eq. (1.6) to the product of the differential cross section for the elastic electron-quark scattering with the probability of finding the quark with momentum fraction between x and $x + \mathrm{d}x$ inside the proton. For the quark of flavour f, let's denote this probability $f^p(x)\mathrm{d}x$. Then $\overline{f}^p(x)$ denotes the probability distribution function for the corresponding antiquark. From this comparison, one gets (summing over possible quark flavours)

$$F_2^{ep}(x) = x \sum_f e_f^2 \left[f^p(x) + \overline{f}^p(x) \right] , \tag{1.7}$$

where e_f is a fraction of elementary charge e of the quark with the flavour f, e.g. $e_f = -1/3$ for s quark. The superscript ep signifies electron-proton scattering. Generally, these $f^p(x)$ functions are called the *parton distribution functions* (PDFs) and are dependent on the type of hadron but not on the type of scattering (which particle is used as a probe), in contrast to the structure functions F_1 and F_2. For example, in the case of electron-proton DIS when neglecting the less probable contributions from heavier sea quarks inside the proton, one can write

$$F_2^{ep}(x) = x \left[\frac{4}{9} \left(u^p(x) + \overline{u}^p(x) \right) + \frac{1}{9} \left(d^p(x) + \overline{d}^p(x) \right) \right] . \tag{1.8}$$

It was discovered that the structure functions generally satisfy the condition $F_2(x) = 2xF_1(x)$, known as Callan-Gross relation, which can be derived under the assumption that the partons are spin-1/2 particles. This ruled out pions as possible candidates for the partons. Similarly, the measurements of the electron-neutron DIS were conducted to attain the data on the neutron structure function $F_2^{en}(x)$, which was then compared with the proton function $F_2^{ep}(x)$. Indeed, the neutron structure function $F_2^{en}(x)$ was found to follow the same scaling behaviour. The detailed calculations based on the combined proton-neutron results clearly spoke in favour of the quark model and confirmed that the partons should be spin-1/2 particles as suggested by Callan and Gross.

More information can be extracted from the $F_2^{ep}(x)$ and $F_2^{en}(x)$ functions by applying the isospin symmetry. This implies that both the proton and the neutron have the same structure with only exchanging the u and d quark, thus $d^n(x) = u^p(x) = u(x)$ and $u^n(x) = d^p(x) = d(x)$. Both structure functions can then be integrated to get two of the so called *sum rules*

$$\int_0^1 F_2^{ep}(x)\mathrm{d}x = \int_0^1 x \left[\frac{4}{9} \left(u(x) + \overline{u}(x) \right) + \frac{1}{9} \left(d(x) + \overline{d}(x) \right) \right] \mathrm{d}x = \frac{4}{9} f_u + \frac{1}{9} f_d , \tag{1.9}$$

$$\int_0^1 F_2^{en}(x)\mathrm{d}x = \int_0^1 x \left[\frac{4}{9} \left(d(x) + \overline{d}(x) \right) + \frac{1}{9} \left(u(x) + \overline{u}(x) \right) \right] \mathrm{d}x = \frac{4}{9} f_d + \frac{1}{9} f_u , \tag{1.10}$$

which can be interpreted as a sum of the total fractional momenta f_u and f_d carried by the corresponding quarks weighted by the squares of their charges. Firstly, these values were found to be equal to $f_u \approx 0.36$ and $f_d \approx 0.18$, thus satisfying $f_u \approx 2f_d$. This indicates that the up quarks carry twice the momentum carried by the down quark, as expected.

Secondly, when adding up the total fractional momenta carried by the valence and the sea quarks in the proton, one arrives at the approximate value of 0.5. This suggests that the rest of the proton momentum must be carried by the neutral gluons which cannot be probed by any scattered lepton because they do not possess electroweak charge. The corresponding gluon distribution function is denoted $g^p(x)$. This "dynamic" result is in contrast with the static idea of the proton structure to be composed solely of *uud* quarks.

A few years later, in 1972, the first results of the neutrino and antineutrino DIS experiments were presented. These were conducted at the 24 GeV Synchrotron in CERN, making use of the large heavy-liquid bubble chamber Gargamelle designed for the detection of neutrinos, and

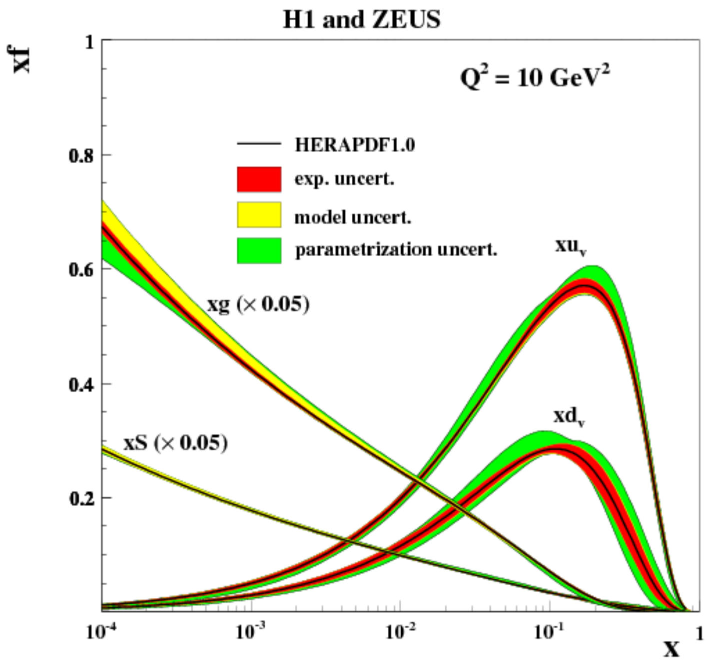

Figure 1.4: PDFs for the proton at $Q^2 = 10$ GeV^2 extracted from HERA data [4]. $S(x)$ stands for the total sea quark contribution. Note that values of the gluon and sea distribution are divided by the factor of 20.

served as an independent verification of the quark model predictions. Since the neutrinos cannot "see" the charge of partons, they are only sensitive to their momentum distribution, meaning the corresponding structure functions take the form

$$F_2^{\nu N}(x) = x \sum_f \left[f^p(x) + \overline{f}^p(x) \right] , \tag{1.11}$$

where f is the quark flavour and N stands for a nucleon. The ratio of F_2^{eN} to $F_2^{\nu N}$ should therefore contain only the information about the fractional quark charges. The quark model predicted this value equals to $\frac{18}{5}$, which was shown to be consistent with the experimental data.

For the sake of completeness, one can end with mentioning the Gross-Llewellyn Smith rule which was also evaluated using Gargamelle results. It is given as the integral of the third structure function $F_3^{\nu N}(x)$ which occurs uniquely in the neutrino-nucleon scattering and its value represents the difference of the number of quarks and antiquarks present in the target nucleon. It was measured to be equal to 3 within the experimental error.

The x-dependence of the proton PDFs as determined at the German electron-proton collider HERA is shown in Fig. 1.4. HERA, operating between 1992 and 2007 was located at DESY in Hamburg and especially two of its experiments, ZEUS and H1, extensively contributed to the measurement of the PDFs and the proton structure functions. In the intermediate-x region ($x \sim 0.1$), it is visible in Fig. 1.4 that the momentum of the proton carried by valence quarks is almost equally distributed among two up and a down valence quark.

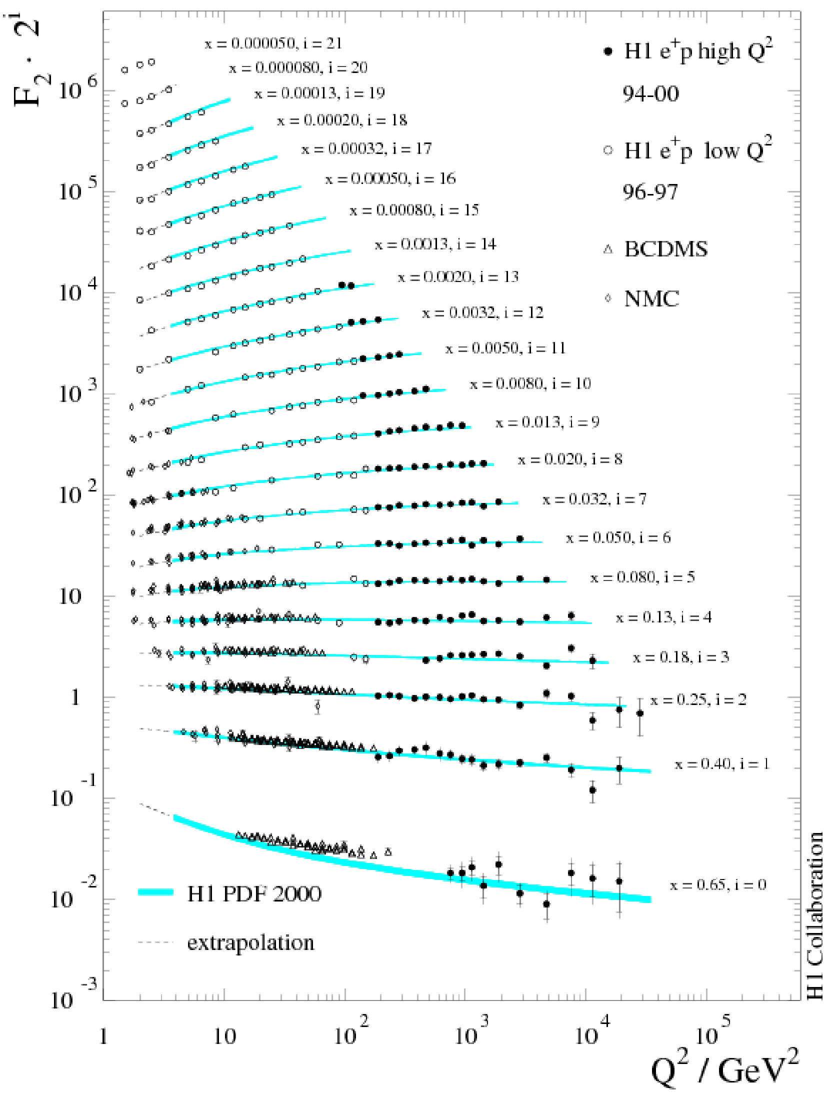

Figure 1.5: Measured values of the F_2 function as a function of Q^2 for different values of the fixed Bjorken x [5].

1.2 Scaling violations

Nonetheless, returning back to Bjorken scaling, it must be noted that it is not an exact phenomenon and is only valid in the specific (Bjorken) limit $q^2 \to \infty$ and $\nu \to \infty$ with the ratio Q^2/ν kept finite. This was later demonstrated in experiments, as shown in Fig. 1.5. The scaling holds in the medium-x region ($x \sim 0.1$) but is clearly violated in the regions of low ($\lesssim 0.05$) and high x ($\gtrsim 0.2$), which were accessed experimentally later on.

The interaction between the quarks and gluons inside the hadrons of course cannot be taken into account in the naive parton model which was formulated before laying the foundations of the QCD theory. But, simply speaking, it is especially this interaction that causes *scaling violations* to occur [6]. Apart from the leading process depicted in Fig. 1.3, where the photon interacts directly with the struck parton, there is a possibility for the parton to first emit a gluon which itself can then fluctuate into a virtual quark-antiquark pair. These are just

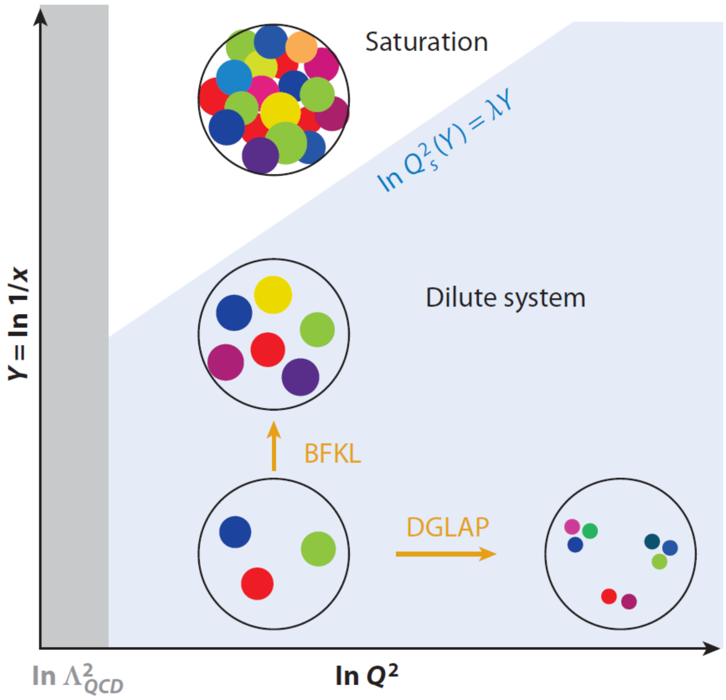

Figure 1.6: The phase diagram of the hadron [7] probed at the virtuality of Q and the rapidity $Y = \ln(1/x)$. The coloured dots denote the partons, Q_s stands for the saturation scale.

prominent examples of possible additional processes. As was already shown in Fig. 1.4, the contribution from gluons and sea quarks becomes significant in the low-x region. On the top of that, the probability of a quark to emit gluons increases with higher values of the squared momentum transfer Q^2. Hence, at small x values, the structure becomes finer as the virtuality Q^2 increases, resulting in a slow rise of the structure function $F_2(x,Q^2)$ [6].

In a similar way, the valence quarks that dominate in the high-x region are again more likely to emit gluons at higher values of Q^2. But the gluon emission generally leads to losses of the quarks' initial momenta, which results in decreasing their x values. This in turn causes a gradual decrease in values of the structure function $F_2(x,Q^2)$ with increasing Q^2 [6], as can be seen in the lower part of Fig. 1.5.

1.3 Gluon saturation

In DIS, one can generally distinguish between two asymptotic limits of QCD dynamics [7]. One of them has been already introduced: it is the Bjorken limit, where $Q^2, \nu \to \infty$ and x remains constant. In this picture, hadrons can be perceived as a dilute system of valence quarks, gluons and $q\bar{q}$ pairs. This is a consequence of the fact that the apparent transverse area of the partons probed by the photon of the virtuality Q^2 scales as $1/Q^2$, so the phase space is sparsely occupied [8]. The Q^2 evolution of the parton distribution functions in this limit can be calculated perturbatively since the strong coupling constant is a monotonically decreasing function of Q. The resulting formula is known as DGLAP (Dokshitzer-Gribov-Lipatov-Altarelli-Parisi) equation [8]. The Q^2 evolution in the Bjorken regime is illustrated by the horizontal arrow at the bottom of Fig. 1.6.

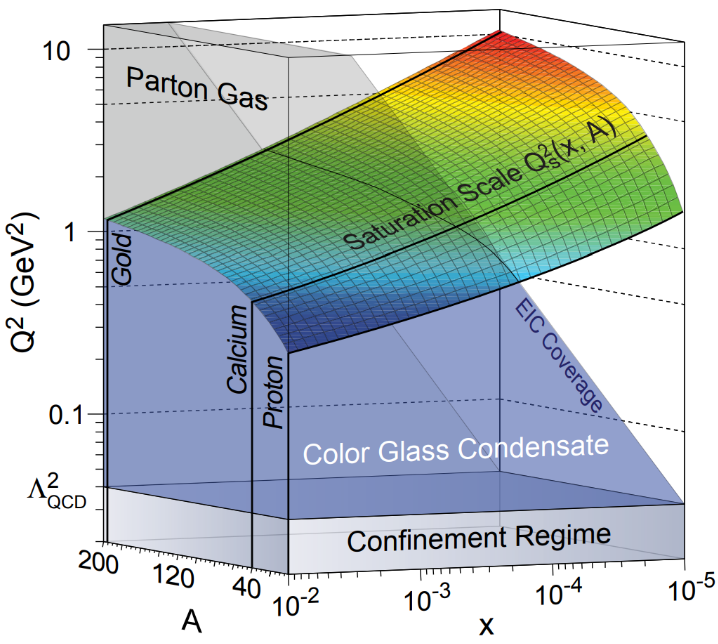

Figure 1.7: The dependence of the saturation scale Q_s on the virtuality of the probe Q, the momentum fraction carried by the parton x and the atomic number A [9].

The latter asymptotic regime is referred to as the Regge-Gribov limit [7] and is reached when Q^2 is fixed and $x \to 0$, corresponding to $s \to \infty$ as suggested by Eq. (1.1). In such a case, it was already shown in Fig. 1.4 that one can neglect everything but gluons, the number of which grows extensively. At some point, it causes the gluons to overlap and the occupation of the phase space begins to saturate. As the theory of the strong interaction allows the gluon self-coupling, the gluons start to recombinate which counteracts the increase in number of partons caused by the energy evolution and leads to the formation of a balanced state. This nonlinear regime of QCD is often referred to as *gluon saturation* [7].

The *saturation scale* Q_s corresponds to momenta at which the nonlinear effects such as gluon recombination start to play a major role [8]. Alternatively, at fixed x, the saturation regime can be achieved by decreasing the virtuality of the probe Q, which increases the apparent size of the probed partons [8]. The energy evolution of the system in the region of low x is given by the BFKL (Balitsky-Fadin-Kuraev-Lipatov) equation [7] and is schematically marked by the arrow pointing upwards in the left part of Fig. 1.6.

The theory describing the hadrons as a dense system of gluons in the infinite momentum frame is known as the Colour Glass Condensate (CGC). One can further note that in the case of heavy nuclei with the atomic number A, the saturation scale depends on $A^{1/3}$ and is thus reached at higher values of Q^2 [7], which is shown in the phase diagram in Fig 1.7.

Chapter 2

Ultra-peripheral collisions

This chapter focuses on the basics of ultra-peripheral collisions and on the motivation to study them. The information was taken from the review by J. G. Contreras and J. D. Tapia Takaki [10], unless stated otherwise.

In ultra-peripheral collisions (UPCs), the participating hadrons a and b collide with an impact parameter b larger than the sum of their radii $R_a + R_b$. Owing to the short range of the strong force, such a distance of course makes any hadronic interaction nearly impossible and the interaction must be mediated by the exchange of virtual photons, source of which are the time-dependent electromagnetic fields generated by the moving projectiles. The approach in which such a field can be replaced by a flux of *equivalent photons* is known as Weizsäcker-Williams approximation, originally developed by Enrico Fermi in 1924 [11].

Since the photon flux created by a fast charged nucleus is proportional to the square of its atomic number Z, a heavy ion (e.g. a lead nucleus at the LHC) is usually used as at least one of the projectiles. The longitudinal size of the projectile is indeed relativistically contracted to R_a/γ_L, giving hadrons a so called pancake shape. Together with the uncertainty principle, this ensures that the maximum possible longitudinal momentum of the coherently emitted photon scales with the Lorentz factor γ_L as $q_{\parallel} \sim \gamma_L/R_a$ [11] and hence increases with the energy of the beam. This means that the centre-of-mass energies of about 500 (1500) GeV in γPb (γp) collisions are achievable at the LHC. One can compare these values to HERA, where the source of the photon was either an electron or a positron and the centre-of-mass energies from 20 to 300 GeV in γp collisions were achieved [12].

The most important processes for this work that can occur in UPCs include either two-photon processes, such as the production of a lepton pair (see the left panel of Fig. 2.1) or vector meson[1] photoproduction (see the right panel of Fig. 2.1) where the photon emitted by one of the nuclei interacts with the second hadron or with one of its constituents. This results in the production of the vector meson which then decays quickly and has to be reconstructed from the decay products. For instance, the mean lifetime of the J/ψ is of the order of 10^{-21} s and one usually reconstructs it from the lepton decay channels (e^-e^+ or $\mu^-\mu^+$, both with corresponding branching ratios of about 6%). Generally, due to the absence of strong hadronic interactions, UPC events are characterised by extremely low multiplicities; in the above examples, the whole detector is empty with the only exception of the produced lepton pair.

[1] The term *vector* refers to mesons with spin 1 and odd parity, as opposed to *pseudovector* mesons with the same spin but even parity. The examples of vector mesons include ρ, ϕ, J/ψ, Υ and others.

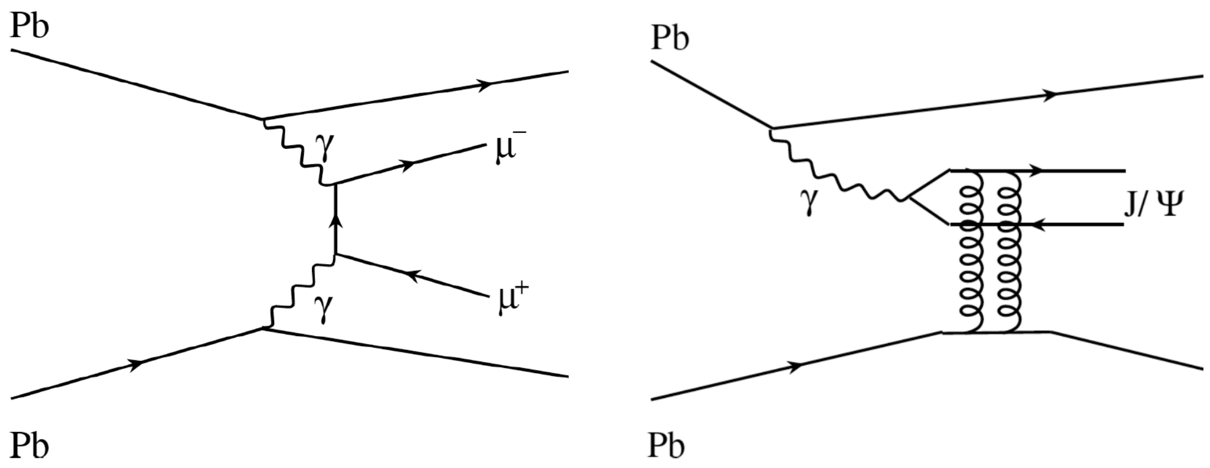

Figure 2.1: Examples of UPC events: production of a lepton pair in a two-photon process (left) and the vector meson photoproduction (right) [10].

2.1 Vector meson photoproduction

The vector meson photoproduction is an important probe in studying the structure of hadrons. It will be shown later in Section 2.4 that in models employing the leading order perturbative QCD (LO pQCD), the differential cross section of the coherent photoproduction is related to the square of the gluon density distribution $g(x,Q^2)$ in the target hadron. As was already pointed out in Eq. (1.1) for the Bjorken-x introduced in DIS, the higher is the centre-of-mass energy of the collision $\sqrt{s}$, the lower is the value of Bjorken-x. In the photoproduction reactions, the vector meson with mass M produced at the rapidity y probes the target hadron structure at

$$x = \frac{M^2}{W^2} = \frac{M}{\sqrt{s}} e^{\pm|y|}\,, \tag{2.1}$$

where W is the centre-of-mass energy of the photon-target hadron system. Here, x can be interpreted as the fraction of the longitudinal momentum transferred from the target hadron [13]. The virtuality scale is usually taken as $Q^2 \sim \frac{M^2}{4}$. In the case of energies at the LHC, the accessible values of the Bjorken-x vary between $\sim 10^{-5}$ and $\sim 10^{-2}$ [14]. At HERA, the corresponding range was roughly $10^{-4} \lesssim x \lesssim 0.02$ [12]. UPCs thus constitute a powerful experimental tool when accessing the low-x region of the hadron structure, where the behaviour of the gluon structure functions and the associated phenomena have to be better understood.

2.1.1 Pb-Pb collisions

Using the method of equivalent photons (EPA), the cross section of the vector meson photoproduction can be factorised into the emission of a virtual photon by a heavy nucleus (the photon flux) and the subsequent interaction of the photon with a target hadron. Considering Pb-Pb collisions, one arrives at the form

$$\frac{\mathrm{d}\sigma_{\mathrm{PbPb}}(y)}{\mathrm{d}y} = n_{\gamma\mathrm{Pb}}(y,\{\boldsymbol{b}\})\sigma_{\gamma\mathrm{Pb}}(y) + n_{\gamma\mathrm{Pb}}(-y,\{\boldsymbol{b}\})\sigma_{\gamma\mathrm{Pb}}(-y)\,, \tag{2.2}$$

symmetry of which originates from the fact that each nucleus can both serve as a source of the exchanged photon or as a target. Here y is again the vector meson rapidity in the laboratory

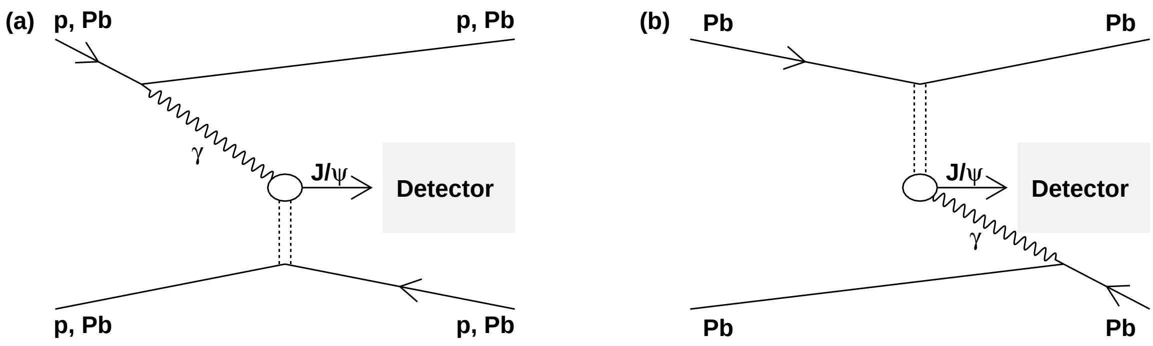

Figure 2.2: Two possible contributions to the photoproduction of the vector meson ([15], modified). The process on the left side corresponds to that with the higher centre-of-mass energy W of the photon-target nucleus system.

reference frame given as $y = \ln(2\omega/M)$, where ω is the photon energy. The term $n_{\gamma\text{Pb}}(y, \{\boldsymbol{b}\})$ denotes the photon flux emitted by a heavy ion, with $\{\boldsymbol{b}\}$ being the impact-parameter range taken into consideration [15].

Because a symmetric heavy-ion ultra-peripheral collision must be treated as a superposition of these two possible contributions, the ambiguity in the centre-of-mass energy $W_{\gamma\text{Pb}}$ of the photon-target ion arises, which was already seen in Eq. (2.1). As the rapidity y of the produced vector meson is defined with respect to the direction in which the target nucleus moves, it can be related to both nuclei and hence two corresponding centre-of-mass energies exist [16], given by

$$W^2_{\gamma\text{Pb}} = \sqrt{s_{\text{NN}}} M e^{\pm|y|} \,, \tag{2.3}$$

where $\sqrt{s_{\text{NN}}}$ is the centre-of-mass energy per nucleon pair. Both situations are depicted in Fig. 2.2, where the process on the left corresponds to that with the higher centre-of-mass energy [15].

When the overall cross section is factorised, one is then left with the cross section $\sigma_{\gamma\text{Pb}}(y)$ describing solely the interaction between the photon and the target hadron. Several approaches that model the photonuclear cross section $\sigma_{\gamma\text{Pb}}(y)$ will be presented in sections 2.3, 2.4, 2.5 and in the following chapter.

In Pb-Pb collisions, one has to distinguish between three types of the photoproduction processes:

- **Coherent**: The coherently emitted photon interacts with the whole nucleus (couples coherently to nearly all the nucleons [17]) and the target nucleus doest not break up. The transverse momentum of the created vector meson is rather low, around $\langle p_\perp \rangle \approx 60\,\text{MeV}/c$.

- **Coherent with nuclear breakup**: If an additional independent photon interaction occurs between the nuclei, which is likely due to their intensive electromagnetic fields, one or both of the nuclei may easily be excited. Then a nuclear breakup can occur, accompanied by the emission of forward neutrons. Measurements showed this accounts for some 30% of the coherent events [17].

- **Incoherent**: In this case the photon interacts quasi-elastically with the inner structure of the nucleus (with a nucleon) and the target nucleus breaks up. This frequently leads to the emission of the forward neutrons or nuclear fragments and the $\langle p_\perp \rangle$ of the produced vector meson can equal to several hundreds of MeV/c. This is closely connected with the difference in the transverse size of a nucleus and of a nucleon [18].

2.1.2 p-Pb collisions

As already suggested, the photoproduction cross section in p-Pb collisions is of the form analogous to Eq. (2.2) except that the proton contribution to the photon flux can be neglected owing to the Z^2-dependence of the number of emitted photons. Thus

$$\frac{\mathrm{d}\sigma_{\mathrm{pPb}}(y)}{\mathrm{d}y} \approx n_{\gamma\mathrm{Pb}}(y,\{\boldsymbol{b}\})\sigma_{\gamma\mathrm{Pb}}(y)\,. \tag{2.4}$$

Analogously to heavy ion collisions, the photoproduction of vector mesons in p-Pb collisions can be categorized as:

- **Exclusive**: The target proton remains intact (it does not break up after the collision) and the mean $\langle p_\perp \rangle$ of the vector meson is roughly 300 MeV/c.
- **Dissociative**: The excitation of the proton occurs, causing it to dissociate, which can lead to production of other particles. The vector meson can be produced with $\langle p_\perp \rangle$ around 1 GeV/c.

2.2 Photon flux

In the Weizsäcker-Williams approach, the photons are coherently emitted by the whole nucleus, which restricts their wavelength to be larger than the size of the nucleus, so that they cannot resolve its inner structure [19]. This coherence condition ensures that the virtuality of such a photon with energy ω and the transerverse momentum $q_\perp$ is rather small,

$$Q^2 = \frac{\omega^2}{\gamma_L^2} + q_\perp^2\,, \tag{2.5}$$

where γ_L is the Lorentz factor of the nucleus. Strictly speaking, the equivalent photon is virtual, however, due to the argument above, it can almost be considered as a real particle, so the expression *quasireal* is often used [19].

One can compute the equivalent photon spectrum $n(\omega)$ describing the number of equivalent photons of a given energy ω coherently emitted by a nucleus with the charge Z as [19]

$$n(\omega) = \frac{\alpha Z^2}{\pi} \int \mathrm{d}^2 q_\perp \frac{q_\perp^2}{\left[\left(\frac{\omega}{\gamma_L}\right)^2 + q_\perp^2\right]^2} F_{\mathrm{el}}^2\left(\left(\frac{\omega}{\gamma_L}\right)^2 + q_\perp^2\right)\,, \tag{2.6}$$

where α is the electromagnetic coupling constant. This expression was derived under the assumption that the emission is elastic (with $F_{\mathrm{el}}(Q^2)$ being the elastic form factor), the nuclear spin is 0 and the plane wave approximation holds [19].

The integral in Eq. (2.6) can be solved analytically if one considers the simplest shape of the form factor, the Heaviside step function $F_{\mathrm{el}}(Q^2) = \Theta(1/R^2 - Q^2)$, where R is the nuclear radius. This effectively cuts off all possible virtualities of the photon beyond the approximate maximum value of $Q^2 \sim 1/R^2$, which results from the condition of coherency. In this case, the approximated form of the equivalent photon spectrum equals [19]

$$n(\omega) = \frac{2\alpha Z^2}{\pi} \ln\left(\frac{\gamma_L}{\omega R}\right) . \tag{2.7}$$

This simplification gives just a basic idea of the shape of the equivalent photon spectrum. One sees that it decreases as $\propto \ln(1/\omega)$ with a cut-off at the maximum energy $\omega_{\max} \approx \gamma_L/R$.

For heavy ions, one can take advantage of the fact that the semi-classical description is applicable [15, 19]. A starting point is the impact parameter-dependent photon flux per unit area

$$n(\omega, \boldsymbol{b}) = \frac{\alpha Z^2}{\pi^2 b^2} u^2 \left[K_1^2(u) + \frac{1}{\gamma_L} K_0^2(u)\right] , \tag{2.8}$$

where $u = \omega b/\gamma_L$ and $K_0(u)$ and $K_1(u)$ are the modified Bessel functions. One can now choose between two approaches to obtain the desired photon flux $n(\omega)$.

The first way is to directly integrate Eq. (2.8) over the possible range of impact parameters, starting from the value $b_{\min}$ which is taken as the sum of the radii of lead ions, $b_{\min} = 2R_{\text{Pb}} \approx$ 14 fm. This rather simple approach is known as *the hard sphere approximation* of the photon flux, since it treats the colliding nuclei as hard spheres and assumes that no hadronic interaction occurs if $b > 2R_{\text{Pb}}$. This procedure is not appropriate for light nuclei [20]. One then arrives at the expression for the photon flux

$$n(\omega) = \int_{b_{\min}}^{\infty} \mathrm{d}^2\boldsymbol{b}\; n(\omega,\boldsymbol{b}) = \frac{2\alpha Z^2}{\pi} \left[\xi K_0(\xi) K_1(\xi) - \frac{\xi^2}{2}\left(K_1^2(\xi) - K_0^2(\xi)\right)\right] , \tag{2.9}$$

where $\xi = \omega b_{\min}/\gamma_L$. In the limit $u \to 0$, it can be shown that this result approaches the logarithmically-decreasing dependence given by Eq. (2.7) [19].

A more sophisticated approach again starts with Eq. (2.8) but uses the convolution of $n(\omega, \boldsymbol{b})$ with the probability $P_{\text{NH}}(b)$ that no hadronic interaction occurs at the impact parameter b [15]. This probability can be obtained employing the Poisson statistics with the mean $T_{\text{AA}}\sigma_{\text{NN}}$, where σ_{NN} is the nucleon-nucleon inelastic cross section and T_{AA} the nuclear overlap function appearing in the Glauber model. T_{AA} can be computed with the nuclear density profile $\rho(r)$ of lead ions approximated by the Woods-Saxon distribution. In this case, the probability of no hadronic interaction exceeds 95% for $b \approx 18$ fm but is essentially zero for $b \lesssim 14$ fm.

Having discussed the electromagnetic part of the photoproduction process, the rest of this chapter is dedicated to the calculation of the photonuclear cross section $\sigma_{\gamma\text{Pb}}(y)$ in which the strong interaction is involved.

2.3 Vector dominance model

The vector meson dominance model (VDM) is based on the fact that the spin, parity and charge conjugation quantum numbers of a photon are the same as those of a vector meson, both equal to $J^{PC} = 1^{--}$. Therefore, if a low-virtuality photon is to fluctuate into a strongly-interacting state (generally a quark-antiquark pair, as indicated in the right panel of Fig. 2.1), the final-state system is likely to be a vector meson [11].

One can decompose the photon wave function into the sum of Fock states [11]

$$|\gamma\rangle = C_{\text{bare}}\,|\gamma_{\text{bare}}\rangle + C_\rho\,|\rho\rangle + C_\omega\,|\omega\rangle + C_\phi\,|\phi\rangle + C_{J/\psi}\,|J/\psi\rangle + \cdots + C_{q\bar{q}}\,|q\bar{q}\rangle\ , \tag{2.10}$$

where $|\gamma_{\text{bare}}\rangle$ corresponds to the bare photon and hence $C_{\text{bare}} \approx 1$. The amplitude C_V is related to the probability that the virtual photon fluctuates into a vector meson state V and is proportional to the inverse of the vector meson-photon coupling f_V, $|C_V| = \sqrt{4\pi\alpha}/f_V$ [11].

Starting with the photonuclear cross section $\sigma_{\gamma\text{Pb}}(y)$, the t-dependence is determined by the nuclear form factor $F(t)$ [20],

$$\sigma_{\gamma\text{Pb}}(y) = \sigma(\gamma + \text{Pb} \to V + \text{Pb}) = \left.\frac{\mathrm{d}\sigma(\gamma + \text{Pb} \to V + \text{Pb})}{\mathrm{d}t}\right|_{t=0} \int_{t_{\min}}^{\infty} \mathrm{d}t\ |F(t)|^2\,, \tag{2.11}$$

where t is the Mandelstam variable describing the momentum transferred to the target nucleus. One can apply the VDM which relates the process $\gamma + \text{Pb} \to V + \text{Pb}$ to $V + \text{Pb} \to V + \text{Pb}$ (assuming that the photon fluctuates into V prior to scattering) and the *optical theorem* that links the forward scattering amplitude to the total vector meson cross section, which yields

$$\left.\frac{\mathrm{d}\sigma(\gamma + \text{Pb} \to V + \text{Pb})}{\mathrm{d}t}\right|_{t=0} = \frac{\alpha\sigma_{\text{tot}}^2(\text{Pb} + V)}{4f_V^2}\,. \tag{2.12}$$

The total Pb + V cross section can be arrived at making use of the classical Glauber model

$$\sigma_{\text{tot}}(\text{Pb} + V) = \int \mathrm{d}^2\boldsymbol{b}\ \left[1 - \exp\left(-\sigma_{\text{tot}}(\text{p} + V)T_{\text{Pb}}(\boldsymbol{b})\right)\right]\,, \tag{2.13}$$

where $\sigma_{\text{tot}}(\text{p} + V)$ is the total vector meson cross section at the proton level and $T_{\text{Pb}}(\boldsymbol{b})$ is the nuclear thickness function. Again, Eq. (2.13) was derived assuming the Poisson probability distribution with $P(\boldsymbol{b}) = \exp(-\sigma_{\text{tot}}(\text{p} + V)T_{\text{Pb}}(\boldsymbol{b}))$ being the probability that no interaction occurs at the given impact parameter.

Applying the optical theorem at the proton level, the total cross section can be expressed in terms of the forward scattering amplitude as

$$\sigma_{\text{tot}}^2(\text{p} + V) = 16\pi \left.\frac{\mathrm{d}\sigma(V + \text{p} \to V + \text{p})}{\mathrm{d}t}\right|_{t=0}\,. \tag{2.14}$$

Lastly, using once more the VDM which at the proton level relates the process $\gamma + \text{p} \to V + \text{p}$ to $V + \text{p} \to V + \text{p}$ yields

$$\left.\frac{\mathrm{d}\sigma(V + \text{p} \to V + \text{p})}{\mathrm{d}t}\right|_{t=0} = \frac{f_V^2}{4\pi\alpha} \left.\frac{\mathrm{d}\sigma(\gamma + \text{p} \to V + \text{p})}{\mathrm{d}t}\right|_{t=0}\,. \tag{2.15}$$

The elementary cross section can be obtained using

$$\left.\frac{\mathrm{d}\sigma(\gamma + \text{p} \to V + \text{p})}{\mathrm{d}t}\right|_{t=0} = b_V\left(X \cdot W_{\gamma\text{p}}^{\epsilon} + Y \cdot W_{\gamma\text{p}}^{-\eta}\right)\,, \tag{2.16}$$

where the energy-dependent form on the right side of Eq. (2.16) is fitted to experimental data with the free parameters X, Y, ϵ, η and b_V. This type of computation is used inside the Starlight Monte Carlo generator, which is widely used in the field.

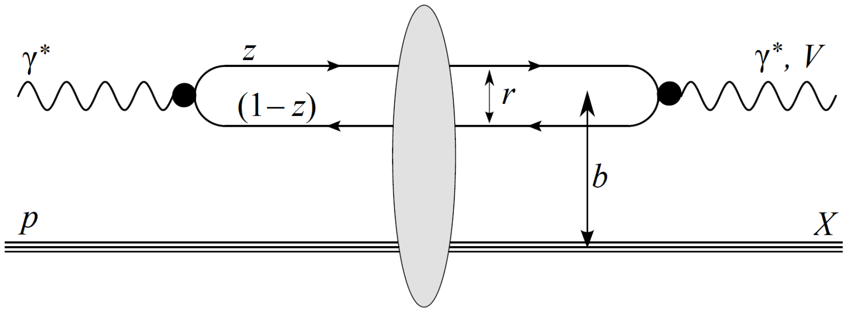

Figure 2.3: Interaction between the colour dipole and the target proton ([8], modified).

2.4 Leading order pQCD

The starting point for the models employing leading order perturbative QCD is also Eq. (2.11) in which the t-dependence is factorised into the nuclear form factor. The forward scattering amplitude is then calculated from a two-gluon exchange as [20]

$$\left.\frac{\mathrm{d}\sigma(\gamma + \mathrm{Pb} \to V + \mathrm{Pb})}{\mathrm{d}t}\right|_{t=0} = \frac{16\pi^3 \alpha_s^2 \Gamma_{ee}}{3\alpha M^5} \left[x g_A \left(x, Q^2 = \frac{M^2}{4} \right) \right]^2 , \tag{2.17}$$

where α_s is the coupling constant of the strong interaction, M still denotes the mass of the vector meson and Γ_{ee} is the decay width of the vector meson to electrons, computation of which requires the wave function of the vector meson to be specified by some model. $g_A(x,Q^2)$ represents the nuclear gluon distribution function, where the virtuality scale is usually chosen as $Q^2 = \frac{M^2}{4}$ as already stated in Section 2.1.

Using the nuclear modification factor of the gluon distribution $R_g(x,Q^2)$ that reflects possible nuclear effects such as gluon shadowing, the nuclear gluon distribution can be related to the gluon PDF in the proton $g_p(x,Q^2)$ measured e.g. by HERA. Then

$$g_A(x,Q^2) = g_p(x,Q^2) R_g(x,Q^2) . \tag{2.18}$$

At small x, the modification factor is lower than 1 whenever the nuclear effects cannot be neglected.

2.5 Colour dipole model

Another method to obtain the forward scattering amplitude is the colour dipole approach in which it is assumed that the photon fluctuates to a colour dipole (a quark-antiquark pair) sufficiently long before the interaction occurs, see Fig. 2.3. The interaction between the dipole and the target hadron is described by the cross section σ_{dip} and it is assumed that no net colour charge is exchanged [13]. Once the interaction takes place, another long time period passes after which the final vector meson is formed.

The main ingredient of the model is the amplitude given by [12, 18]

$$A(x,Q^2,\boldsymbol{\Delta})_{T,L} = i \int \mathrm{d}\boldsymbol{r} \int_0^1 \frac{\mathrm{d}z}{4\pi} \, [\Psi^* \Psi_V]_{T,L} \int \mathrm{d}\boldsymbol{b} \, e^{-i(\boldsymbol{b}-(1-z)\boldsymbol{r})\cdot\boldsymbol{\Delta}} \left(\frac{\mathrm{d}\sigma_{\mathrm{dip}}}{\mathrm{d}\boldsymbol{b}} \right) , \tag{2.19}$$

where

- the transverse momentum $\boldsymbol{\Delta}$ is related to the momentum transfer t through $-t = \boldsymbol{\Delta}^2$,
- $\boldsymbol{r}$ stands for the transverse size of the dipole (r is the distance between the quark and the antiquark),
- z denotes the fraction of the photon momentum which is carried by the quark,
- Ψ is the wave function of the virtual photon splitting into the dipole as $\gamma^* \to q\bar{q}$,
- Ψ_V is the wave function of the vector meson and
- σ_{dip} is the *colour dipole-target cross section*, which carries information about the physics of the process and has to be provided by a specific model (see Chapter 3).

Following a Good-Walker formalism, the cross section for the exclusive/coherent photoproduction is found to be proportional to the square of the average over different target configurations given by the amplitude $A(x, Q^2, \boldsymbol{\Delta})_{T,L}$, i.e. [12, 18]

$$\left.\frac{\mathrm{d}\sigma(\gamma + \mathrm{p/Pb} \to V + \mathrm{p/Pb})}{\mathrm{d}t}\right|_{T,L}^{\mathrm{exc/coh}} = \frac{(R_g^{T,L})^2}{16\pi} \left|\left\langle A(x, Q^2, \boldsymbol{\Delta})_{T,L}\right\rangle\right|^2 , \tag{2.20}$$

while the dissociative/incoherent photoproduction cross section is sensitive to the variance over target configurations [12, 18]

$$\left.\frac{\mathrm{d}\sigma(\gamma + \mathrm{p/Pb} \to V + \mathrm{X/Pb})}{\mathrm{d}t}\right|_{T,L}^{\mathrm{dis/inc}} = \frac{(R_g^{T,L})^2}{16\pi} \left[\langle|A(x, Q^2, \boldsymbol{\Delta})_{T,L}|^2\rangle - |\langle A(x, Q^2, \boldsymbol{\Delta})_{T,L}\rangle|^2\right] , \tag{2.21}$$

where the subscripts T,L represent the contributions of transversely and longitudinally polarised virtual photons and X denotes the product after the dissociation of the proton. One can easily notice that with no fluctuations in the target configurations, the variance vanishes and the dissociative/incoherent cross section is zero [13].

The term $R_g^{T,L}$ is called the *skewedness correction* and is defined as [18]

$$R_g^{T,L}(\lambda_g^{T,L}) = \frac{2^{\lambda_g^{T,L}+3}}{\sqrt{\pi}} \frac{\Gamma(\lambda_g^{T,L} + 5/2)}{\Gamma(\lambda_g^{T,L} + 4)} , \tag{2.22}$$

where Γ is the gamma function and the parameter $\lambda_g^{T,L}$ equals

$$\lambda_g^{T,L} = \frac{\partial \ln(A_{T,L})}{\partial \ln(1/x)} . \tag{2.23}$$

The skewedness correction takes into consideration that there are two gluons mediating the interaction between the colour dipole and the hadronic target (see the right panel of Fig. 2.1) and different values of Bjorken x are assigned to each of them, but only a single value of x is used in the calculation.

Chapter 3

Energy-dependent hot-spot model

In this chapter, an energy-dependent hot-spot model developed by J. Čepila, J. G. Contreras and J. D. Tapia Takaki is introduced. It represents one of the options to determine the dipole-target cross section σ_{dip}.

One of the crucial assumptions of the model is that the transverse profile of the target hadron is fluctuating. To see the importance of the geometric fluctuations, Section 3.1 at first reviews the analysis by H. Mäntysaari and B. Schenke [13] dedicated to this topic.

A hot-spot model was originally applied to the J/ψ photoproduction in γ-p collisions where the fluctuating transverse profile of the proton is described as a sum of high-gluon-density *hot spots*, the number of which grows with the decreasing Bjorken-x. A summary of this study [12] can be found in Section 3.2. The extension of the model to the case of A-A collisions (the photonuclear production) [18] is presented afterwards in Section 3.3.

Although the model employs a rather simple description of the transverse hadron structure, it succeeds in correctly describing the J/ψ photoproduction cross sections and provides experimentally attractive predictions, as will be demonstrated later.

3.1 Fluctuating hadron structure

Using the optical theorem, the dipole-proton cross section introduced in Eq. (2.19) can be related to the imaginary part of the forward dipole-target amplitude $N(x,\boldsymbol{r},\boldsymbol{b})$ by

$$\frac{\mathrm{d}\sigma_{\mathrm{dip}}}{\mathrm{d}\boldsymbol{b}} = 2N(x,\boldsymbol{r},\boldsymbol{b})\,. \tag{3.1}$$

The amplitude N satisfies the impact parameter dependent Balitsky-Kovchegov (BK) equation but, as pointed out in [13], it can have unphysical Coulomb tails which must be compensated for. The authors chose two methods, namely the impact parameter dependent saturation model (IPsat) and the IP-Glasma model, to extract the dipole-target cross section.

In both models, the geometric fluctuations are inserted by replacing the Gaussian-shaped proton's spatial profile in the impact parameter plane

$$T_p(\boldsymbol{b}) = \frac{1}{2\pi B_p}\exp\left(-\frac{\boldsymbol{b}^2}{2B_p}\right) \tag{3.2}$$

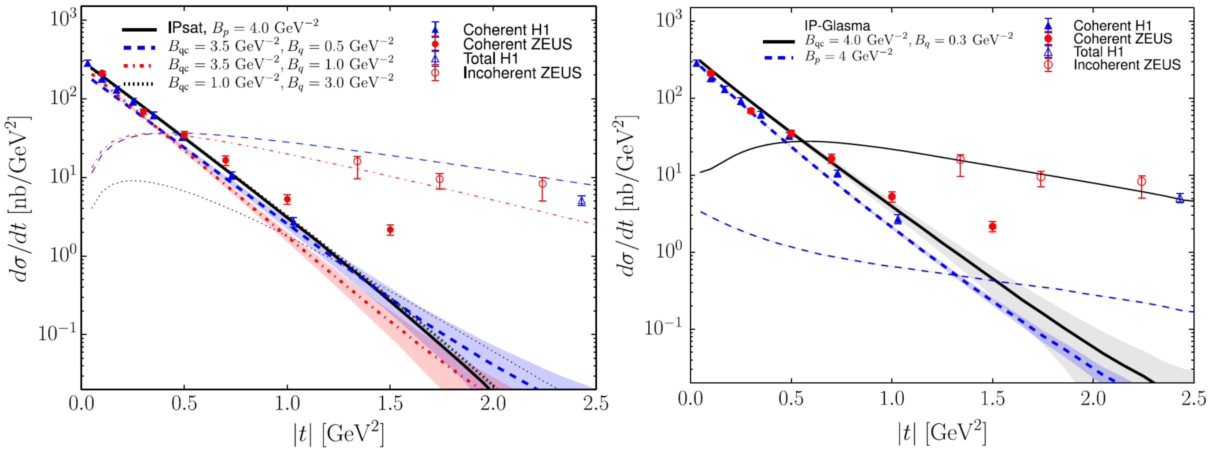

Figure 3.1: The exclusive (thick lines) and dissociative (thin lines) J/ψ photoproduction cross sections calculated within the IPsat (left) and IP-Glasma (right) model with different parameters of the proton structure [13]. Results are compared with HERA data.

with the sum over the valence quarks

$$T_p(\boldsymbol{b}) \rightarrow \frac{1}{N_q}\sum_{i=1}^{N_q} T_q(\boldsymbol{b}-\boldsymbol{b}_i), \tag{3.3}$$

where $N_q = 3$ and each quark itself is assumed to be of a Gaussian shape

$$T_q(\boldsymbol{b}) = \frac{1}{2\pi B_q}\exp\left(-\frac{\boldsymbol{b}^2}{2B_q}\right). \tag{3.4}$$

The parameters B_i denote the widths of the corresponding distributions. For the round proton without any substructure, it is conventionally taken as $B_p = 4.0$ GeV^{-2}. The fluctuations are encoded in the positions of quarks $\boldsymbol{b}_i$ which are randomly sampled from a Gaussian distribution centred at $(0, 0)$ and of a width B_{qc}. The gluons are supposed to be radiated by large-x valence quarks, therefore are scattered around $\boldsymbol{b}_i$ positions. In addition, fluctuations of the proton saturation scale $Q_s(\boldsymbol{b},x)$ from event to event can be introduced.

Using the IPsat and IP-Glasma models, the authors in [13] calculated the $|t|$-dependent exclusive and dissociative cross sections of the J/ψ photoproduction and made a comparison with data from HERA experiments H1 and ZEUS. Here t is the momentum transfer between the incoming and outgoing proton. Resulting plots can be found in Fig. 3.1.

As apparent from results of the IPsat model, a smoother proton structure with larger valence quarks ($B_q = 3.0$ GeV^{-2}) sampled relatively close to each other ($B_{qc} = 1.0$ GeV^{-2}) succeeds in describing the exclusive cross section but fails completely in predicting the measured values of the dissociative cross section. The model of a round proton ($B_p = 4.0$ GeV^{-2}) gives a very similar dependence of the exclusive cross section but cannot provide non-zero dissociative cross section as the fluctuatins are not present, resulting in zero variance over target configurations in Eq. (2.21).

To reach an accordance of the modelled dissociative cross section with experimental results, the need for large geometric fluctuations ($B_{qc} = 3.5$ GeV^{-2}) with narrower valence quark centres ($B_q \simeq 0.5$ GeV^{-2}) is evident. This conclusion is further supported by examining the results of the IP-Glasma model in the right panel of Fig. 3.1. It should be noted here that the round proton structure produces non-zero dissociative cross section in the IP-Glasma model in contrast to the former which is a consequence of additional colour charge fluctuations.

3.2 Energy dependent hot-spot model: γ-p collisions

The key ideas of an energy-dependent hot-spot model are two:

- The fluctuating proton structure is described in terms of high-gluon-density hot spots rather than the valence quarks so that the condition $N_q = 3$ is no longer restricting.
- An energy dependence of the proton profile $T_p(\vec{b})$ is then introduced indirectly by assuming that the number of hot spots $N_{hs}(x)$ is a decreasing function of x, i.e. grows with decreasing x. At fixed scale Q^2, this reflects the surmise that the number of gluons that can participate in the interaction grows with increasing energy of the collision, as illustrated in Fig. 1.6 in the region of low Q^2.

The authors in [12] followed a similar procedure starting with Eq. (3.1). From the forward dipole-target amplitude, one can factorise the proton profile $T_p(\boldsymbol{b})$ so that

$$N(x,\boldsymbol{r},\boldsymbol{b}) = \sigma_0 N(x,r) T_p(\boldsymbol{b})\,, \tag{3.5}$$

where σ_0 is a normalisation constant and the dependence on the remaining variables x and $\boldsymbol{r}$ is encoded in $N(x,r)$. One possibility is to set

$$N(x,r) = \left[1 - \exp\left(-r^2 Q_s^2(x)\right)\right]\,, \tag{3.6}$$

where the saturation scale is given by $Q_s^2(x) = Q_0^2(x_0/x)^\lambda$, Q_0^2, x_0 and λ are free parameters to be fitted to experimental data.

Similarly as in Eq. (3.3) and (3.4), the proton profile with Gaussian-distributed hot spots is introduced as

$$T_p(\boldsymbol{b}) = \frac{1}{N_{hs}} \sum_{i=1}^{N_{hs}} T_{hs}(\boldsymbol{b} - \boldsymbol{b}_i)\,, \tag{3.7}$$

where individual hot spots themselves are of a Gaussian shape

$$T_{hs}(\boldsymbol{b} - \boldsymbol{b}_i) = \frac{1}{2\pi B_{hs}} \exp\left(-\frac{(\boldsymbol{b} - \boldsymbol{b}_i)^2}{2B_{hs}}\right)\,. \tag{3.8}$$

Again, the positions of hot spots $\boldsymbol{b}_i$ are sampled from 2-dimensional Gaussian distribution with a width of B_p centred at $(0, 0)$.

Using all the above mentioned assumptions, the computation of the dipole amplitude $A(x,Q^2,\boldsymbol{\Delta})_{T,L}$ was performed. Eventually, the energy evolution of $N_{hs}(x)$ was chosen to be

$$N_{hs}(x) = p_0 x^{p_1}(1 + p_2\sqrt{x})\,, \tag{3.9}$$

with three parameters p_i which were set to $p_0 = 0.011$, $p_1 = -0.58$ and $p_2 = 250$ by making a comparison to data from H1 on the dissociative J/ψ photoproduction. Other parameters were constrained to values $\lambda = 0.21$, $x_0 = 2 \times 10^{-4}$, $B_p = 4.7$ GeV^{-2} and finally the size of hot spots

$B_{hs} = 0.8\,\text{GeV}^{-2}$. The vector meson wave function Ψ_V was obtained using the boosted-Gaussian model.

Apart from computing the exclusive and dissociative cross sections, the authors also used the model to calculate the F_2 proton structure function for which the form

$$F_2(x,Q^2) = \frac{Q^2}{4\pi^2\alpha}\left(\sigma_T^{\gamma^* p}(x,Q^2) + \sigma_L^{\gamma^* p}(x,Q^2)\right), \tag{3.10}$$

was employed, where T, L denote the virtual photon polarization, α is the fine structure constant and the virtual photon-proton cross sections were obtained as

$$\sigma_{T,L}^{\gamma^* p}(x,Q^2) = \sigma_0 \int d\boldsymbol{r} \int_0^1 dz\, |\Psi_{T,L}(z,r,Q^2)|^2 N(r,\tilde{x})\,, \tag{3.11}$$

where $\tilde{x} = x(1 + (4m_f^2)/Q^2)$ with an effective mass of the light quarks $m_f \simeq 140$ MeV.

3.2.1 Results

The left panel of Fig. 3.2 shows the comparison of the calculated $F_2(x,Q^2)$ structure function with the data measured by H1 and ZEUS at the scale $Q^2 = 2.7\,\text{GeV}^2$, which is comparable to the virtuality scale usually taken as $M^2/4 \simeq 2.4\,\text{GeV}^2$ when talking about the J/ψ photoproduction. The fact that the model is in relatively good accordance with the data is an important byproduct since the model was designed primarily for describing the vector meson photoproduction cross sections.

The right side of Fig. 3.2 illustrates the calculated $|t|$-dependence of the exclusive and dissociative cross sections. Comparison is made with H1 data collected at the energy of $\langle W_{\gamma p}\rangle =$ 78 GeV. One can notice that at large $|t|$, the total cross section computed within this model is purely dissociative to a good accuracy [13].

Finally, the energy dependence of the exclusive and dissociative cross sections compared with data by H1 and ALICE (p-Pb at a centre-of-mass energy of 5.02 TeV) are depicted in Fig. 3.3. Apart from describing well the experimental data, one can see that the model predicts a saturation of the dissociative cross section at a maximum value of roughly 90 nb at $\langle W_{\gamma p}\rangle \approx 500$ GeV, which is followed by a steep decrease for higher energies.

This prediction can be explained as follows: at the energy $\langle W_{\gamma p}\rangle \approx 500$ GeV, approximately 10 hot spots are present in the proton and as $B_{hs} = 0.8\,\text{GeV}^{-2}$ corresponds to the radius of 0.35 fm, this represents a significant overlap between the hot spots. As a result, the variance begins to decrease as target configurations increasingly resemble each other with further increasing the energy. An important conclusion is that the region of $\langle W_{\gamma p}\rangle \approx 500$ GeV is indeed reachable in p-Pb collisions at the LHC, making it suitable to search for such a signature of the gluon saturation.

3.3 Energy dependent hot-spot model: Pb-Pb collisions

The authors in [18] employed two approaches to determine the dipole-nucleus cross section $\frac{\mathrm{d}\sigma_{\text{dip}}}{\mathrm{d}\boldsymbol{b}}$ appearing in Eq. (2.19). The former is referred to as geometric scaling (GS) since the saturation scale of a proton is geometrically scaled to the nucleus with the mass number A, while the latter

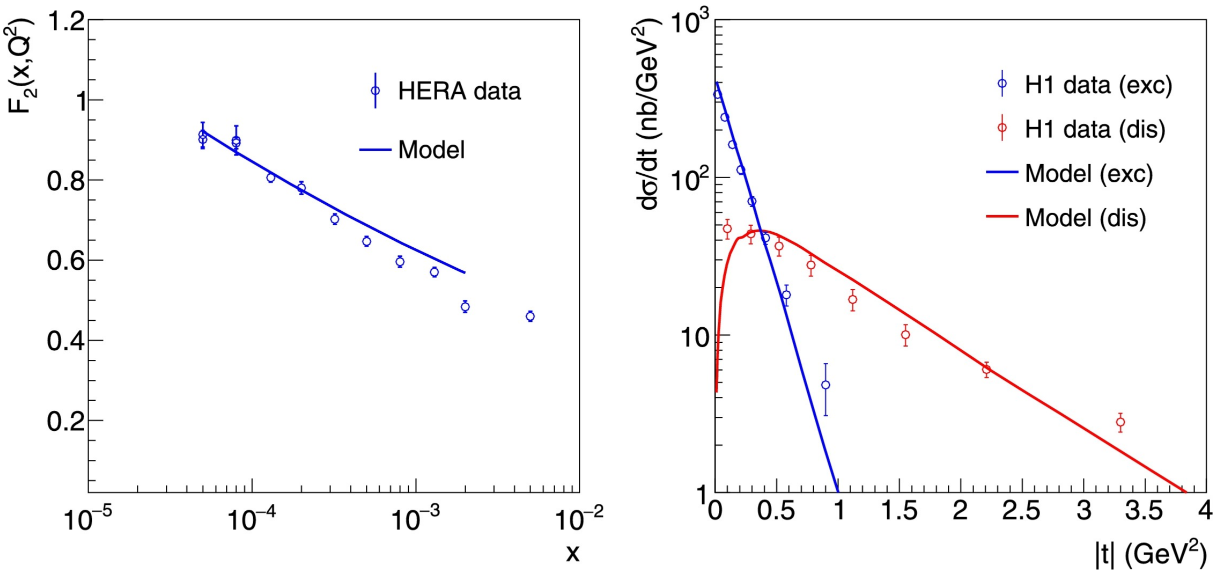

Figure 3.2: The calculated dependence of the proton structure function $F_2(x,Q^2)$ on Bjorken x compared with data by HERA (left) at $Q^2 = 2.7$ GeV^2 [12]. The modelled $|t|$-dependence of the exclusive and incoherent cross sections in a comparison with H1 data (right) at the energy of $\langle W_{\gamma p} \rangle = 78$ GeV [12].

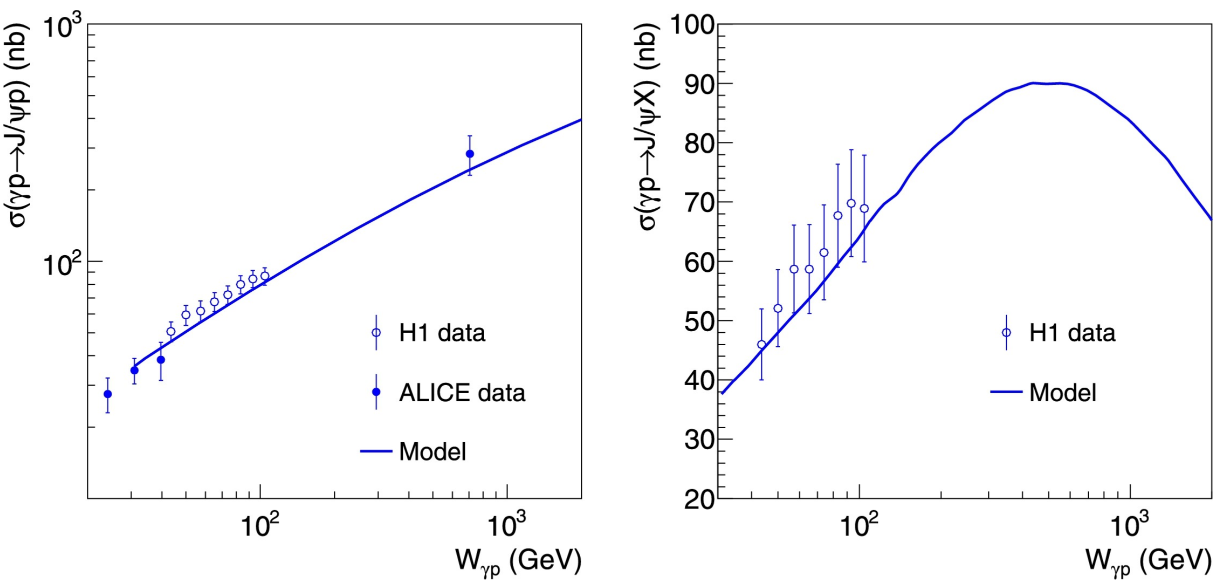

Figure 3.3: Energy dependence of the calculated exclusive (left) and dissociative (right) photoproduction cross sections compared with experimental data from H1 and ALICE [12].

is known as Glauber-Gribov (GG) formalism. Again, the fluctuating subnucleonic hot-spot structure is implemented in the nuclear profile function $T_A(\boldsymbol{b})$, which will be introduced later on.

When working with the GS model, the x and $\boldsymbol{b}$ dependences of the dipole-nucleus cross section are factorised as

$$\frac{\mathrm{d}\sigma_{\mathrm{dip}}}{\mathrm{d}\boldsymbol{b}} = \sigma_0^A \left[1 - \exp\left(-r^2 Q_{A,s}^2(x)/4\right)\right] T_A(\boldsymbol{b}), \tag{3.12}$$

where σ_0^A is the normalisation constant, which is connected with the transverse area of the target nucleus by $\sigma_0^A = \pi R_A^2$. The nuclear radius R_A is a parameter of the Woods-Saxon distribution. Finally, the geometric scaling of the proton saturation scale Q_s^2 gives for the nuclear saturation scale

$$Q_{A,s}^2(x) = Q_s^2 \left(\frac{A\pi R_p^2}{\pi R_A^2}\right)^{1/\delta}, \tag{3.13}$$

where the ratio $A\pi R_p^2/\pi R_A^2$ describes the difference in the transverse area of the nucleus with respect to simply counting the transverse area of the proton A times. The exponent δ was set to 0.8.

On the other hand, the GG approach uses the cross section of the dipole-proton interaction $\sigma_{\mathrm{dip},p}$ to express that of dipole-nucleus interaction,

$$\frac{\mathrm{d}\sigma_{\mathrm{dip}}}{\mathrm{d}\boldsymbol{b}} = 2\left[1 - \exp\left(-\frac{1}{2}\sigma_{\mathrm{dip},p}(x,r) T_A(\boldsymbol{b})\right)\right]. \tag{3.14}$$

Here the dipole-proton cross section is modelled as

$$\sigma_{\mathrm{dip},p}(x,r) = \sigma_0 \left[1 - \exp\left(-r^2 Q_s^2(x)/4\right)\right] \tag{3.15}$$

and is related to σ_{dip} by the nuclear profile $T_A(\boldsymbol{b})$. The normalisation constant is equal to the transverse area of the proton $\sigma_0 = \pi R_p^2$, where R_p is a radius of the proton. The x-dependence of the saturation scale of the proton is given by

$$Q_s^2(x) = Q_0^2 \left(\frac{x_0}{x}\right)^{\lambda}, \tag{3.16}$$

where Q_0^2, x_0 and λ are parameters.

The nuclear profile was chosen either to neglect any subnucleonic structure, considering the nucleus to be comprised of A nucleons only, or to include hot spots as subnucleonic degrees of freedom. These cases are denoted by -n or -hs in the presented figures. The former case corresponds to the nuclear profile of the form

$$T_A(\boldsymbol{b}) = \frac{1}{2\pi B_p} \sum_{i=1}^{A} \exp\left(\frac{(\boldsymbol{b} - \boldsymbol{b}_i)^2}{2B_p}\right), \tag{3.17}$$

where each nucleon is of a Gaussian profile of the width B_p and the positions of the nucleons $\boldsymbol{b}_i$ are sampled from the corresponding Woods-Saxon distribution. In the latter case, the nuclear profile equals

$$T_A(\boldsymbol{b}) = \frac{1}{2\pi B_{hs}} \sum_{i=1}^{A} \frac{1}{N_{hs}} \sum_{k=1}^{N_{hs}} \exp\left(\frac{(\boldsymbol{b} - \boldsymbol{b}_i - \boldsymbol{b}_k)^2}{2B_{hs}}\right). \tag{3.18}$$

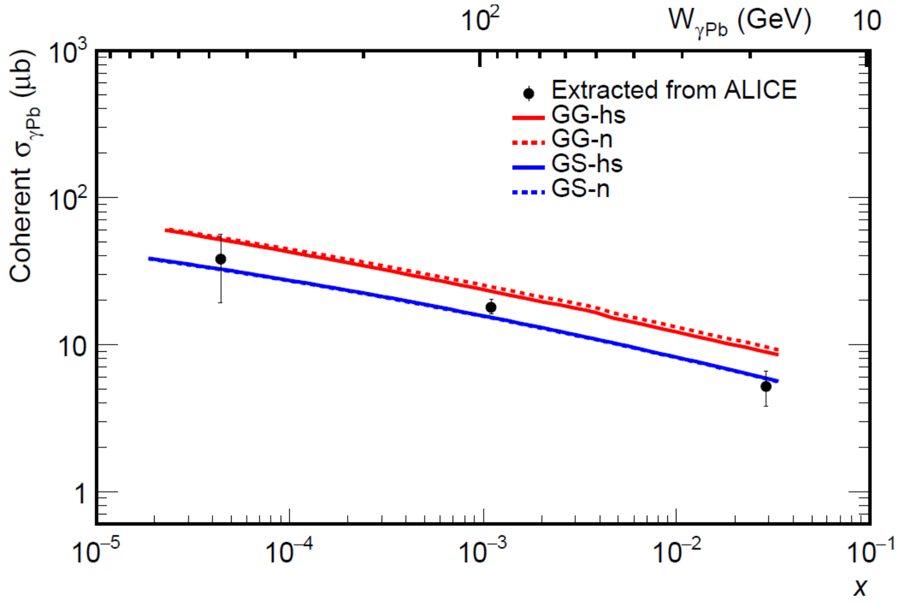

Figure 3.4: The modelled x ($W_{\gamma\mathrm{Pb}}$) dependence of the cross section of the coherent photoproduction of J/ψ in lead-lead collisions compared with data by ALICE [18].

Here the Gaussian-shaped hot spots with a width of B_{hs} are distributed at positions $\boldsymbol{b}_k$ around the original positions $\boldsymbol{b}_i$ of the nucleons. The factor $1/N_{hs}$ provides a proper normalisation, so that still

$$\int T_A(\boldsymbol{b})d\boldsymbol{b} = A\,. \tag{3.19}$$

At a given x, the number of hot spots in each nucleon is obtained from the Poisson distribution with a mean value of

$$\langle N_{hs}(x)\rangle = p_0 x^{p_1}(1 + p_2\sqrt{x})\,, \tag{3.20}$$

with all the parameters set to the same values as in Section 3.2.

The advantage of the GS approach lies in the fact that the integrals over the impact-parameter space can be solved analytically, while the integrals in the GG formalism have to be computed numerically on a grid in the impact-parameter space.

3.3.1 Results

Computations were performed at the virtuality scale of $Q^2 = 0.05$ GeV^2 and the boosted-Gaussian model was used to obtain the wave function of the vector meson.

In Fig. 3.4 and 3.5, one can find the predictions of the hot-spot model on the x-dependent coherent and incoherent cross section, compared with the data collected by ALICE during Run 1 (2009-2013) at the LHC. In the presented range of x, the GS method describes the data better than the GG version of the model, which slightly overestimates the values across the whole range. Similarly as before, the coherent process is almost insensitive to the inclusion of the subnucleonic degrees of freedom. A small difference between the predictions of GG-n and GG-hs results from the usage of the grid when computing integrals over the impact parameter $\boldsymbol{b}$.

Nevertheless, the results of the model in the case of the incoherent process show that a difference in the predicted values arises when the hot-spot substructure of nucleons is included,

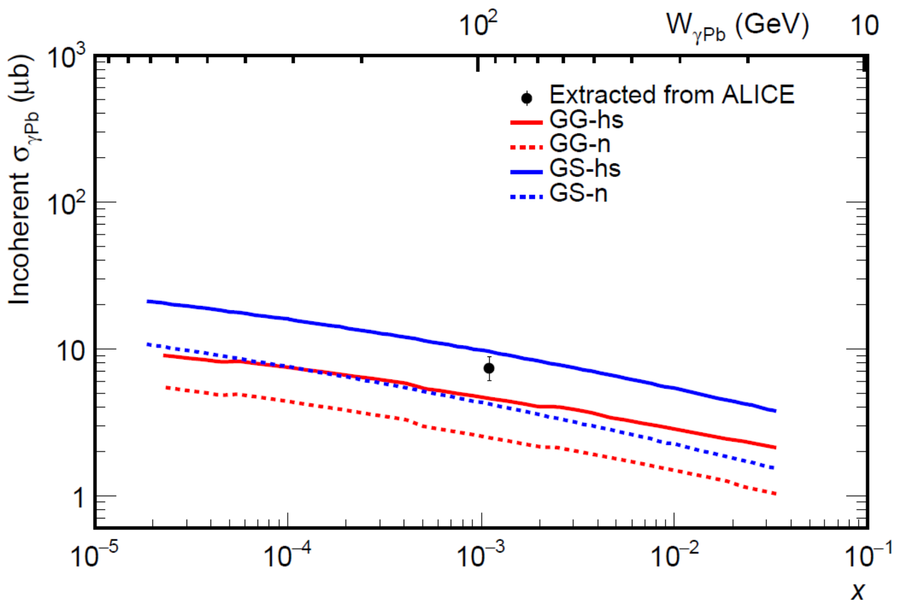

Figure 3.5: The modelled x ($W_{\gamma\mathrm{Pb}}$) dependence of the cross section of the incoherent photoproduction of J/ψ in lead-lead collisions compared with data by ALICE [18].

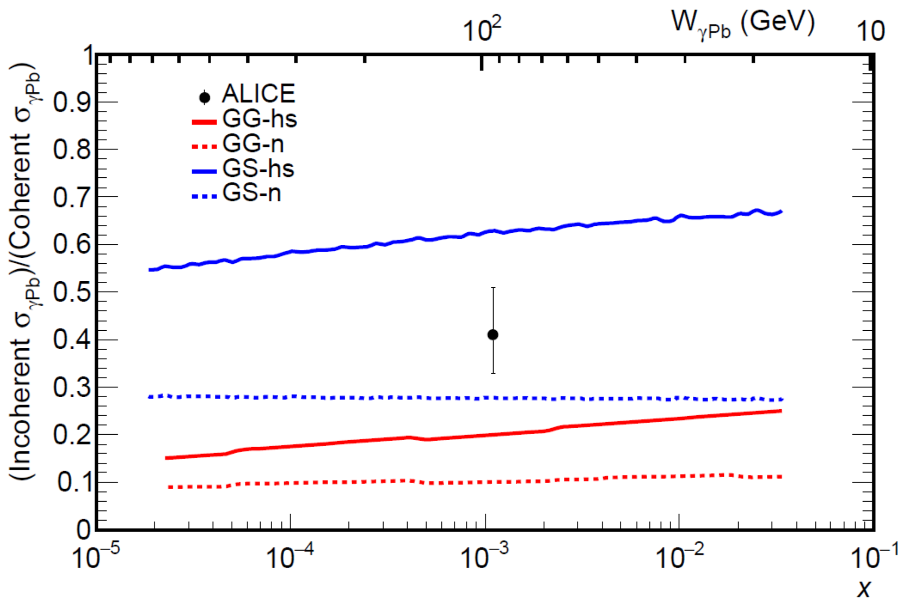

Figure 3.6: The modelled ratio of the incoherent to coherent cross section describing the photonuclear production of J/ψ in lead-lead collisions [18]. Predictions are compared with data by ALICE.

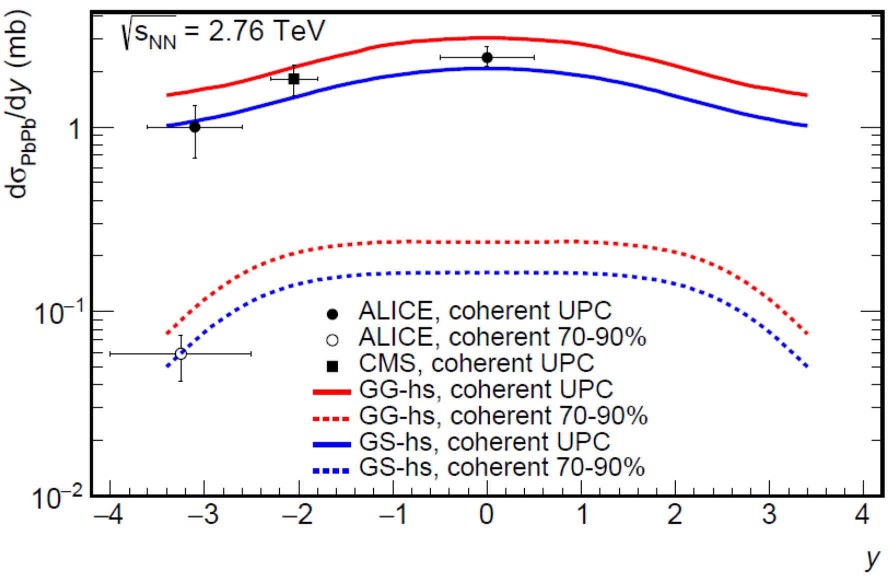

Figure 3.7: The modelled y-dependence of the cross section of the coherent photoproduction of J/ψ in lead-lead collisions compared with data by ALICE and CMS [18].

as evident from Fig. 3.5. Moreover, it seems that the nuclear profile with hot spots gives a better description of the data in case of both the GS and GG models.

An important tool to assess the suitability of the hot-spot model is the calculation of the ratio of the coherent and incoherent cross sections, which would be a constant function of x if one neglects the subnucleonic structure, but becomes an increasing function of x if the hot spots are included. This is a key consequence of Eq. (3.20) that introduces the energy dependence of the number of hot spots. A combination of results gathered by ALICE ($x \approx 0.001$) and PHENIX at RHIC ($x = 0.015$, not shown in the figure) supports the surmise that the ratio evolves with energy. However, the lack of experimental data causes that one cannot come to a conclusion before further results on the incoherent cross section are delivered, which constitutes one of the motivations for the study presented in this thesis.

Lastly, taking into account that the hot-spot nuclear profile proved to be in a better agreement with the experimental results, the authors used the GS-hs and GG-hs models to describe the y-dependent photonuclear cross section as defined by Eq. (2.2) for various centrality classes. The comparison with data by ALICE and CMS at the Run 1 centre-of-mass energy of $\sqrt{s_{\mathrm{NN}}} = 2.76$ TeV on the coherent (incoherent) photoproduction is shown in Fig. 3.7 (3.8). One can observe that the GS is in a noteworthy accordance with the data and a tendency of the GG version to mildly overestimate the measured values is preserved. The authors also made predictions of the y-dependence of the cross section for the centre-of-mass energy of 5.02 TeV corresponding to the LHC Run 2 (2015-2018) which are not shown in this study, but could be later compared with the analysed results, which are expected to have lower uncertainties.

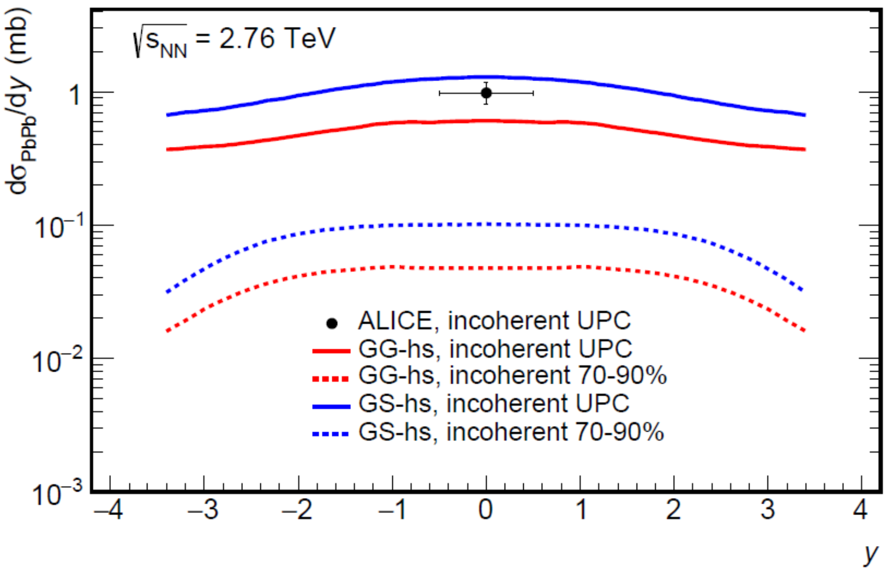

Figure 3.8: The modelled y-dependence of the cross section of the incoherent photoproduction of J/ψ in lead-lead collisions compared with data by ALICE and CMS [18].

Chapter 4

ALICE

The Large Hadron Collider (LHC) is a hadron synchrotron located at the European Organization for Nuclear Research (CERN) in Geneva. It constitutes the last stage of the CERN accelerator chain and is situated in a circular tunnel with a circumference of 26.7 km, 45-175 m underground [21]. The tunnel was originally built for the Large Electron–Positron Collider (LEP).

Measurements at LEP were taken between the years 1989 and 2000, after which the machine was dismantled. Since one of the initial goals of the LEP collider was to gather new data on Z^0 decay, the energy of beams equalled approximately 45 GeV (about half the invariant mass of the Z^0 boson) till 1995 [22]. Thanks to numerous following upgrades, the beam energies reached the value of 104.4 GeV by the year 2000, which makes LEP the highest energy lepton collider ever constructed [22].

The LHC was primarily constructed to collide proton beams with a designed centre-of-mass energy of 14 TeV and a luminosity reaching 10^{34} cm^{-2}s^{-1} [21]. The first proton collision took place in November 2009. Besides, the LHC is also used to collide lead ions for which the designed parameters are equal to 5.6 TeV (centre-of-mass energy per nucleon pair) and 10^{27} cm^{-2}s^{-1} (peak luminosity) [21]. Particles are injected from the Super Proton Synchrotron (SPS), whose output beam energies are 450 GeV for protons and 177 GeV per nucleon for lead ions [21].

So far, the centre-of-mass energies of 13 and 5.02 TeV have been achieved at the LHC for proton-proton and lead-lead collisions respectively. Since December 2018, the LHC undergoes the Long Shutdown 2, projected to end in 2021. During this time, several important upgrades will be performed, which are crucial for the implementation of the High Luminosity LHC project in 2026.

A Large Ion Collider Experiment (ALICE) is one of the four main experiments operating at the LHC, together with ATLAS, CMS and LHCb. It is a general-purpose detector intended to study strongly interacting matter and to explore properties of the quark-gluon plasma (QGP). The following information about the experiment presented in this chapter is taken from [23], unless stated otherwise.

4.1 The ALICE detector layout

The ALICE detector is located in a cavern of $26 \times 16 \times 16$ m^3, which lies 56 m beneath the ground and which was previously occupied by the L3 experiment at LEP. The whole ALICE apparatus

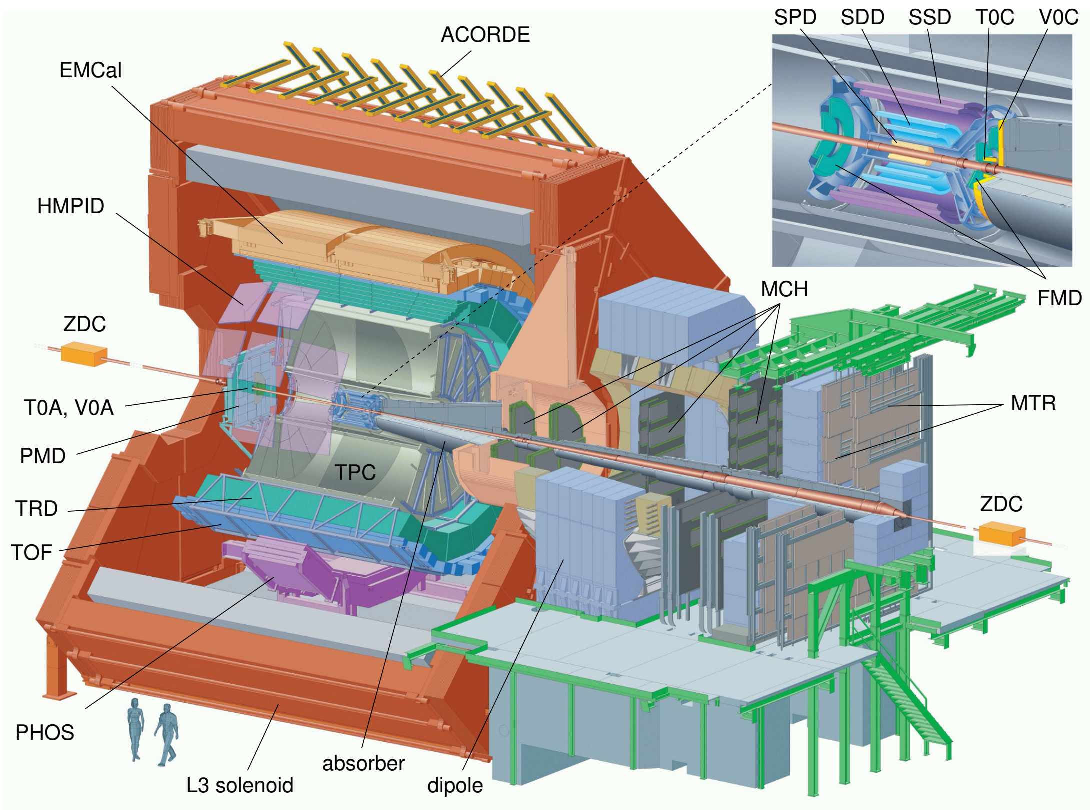

Figure 4.1: Scheme of the ALICE detector set-up during Run 1 (2009-2013) [24].

weighs around 10 000 t. ALICE makes use of a huge solenoid magnet with an octagonal cross section, whose magnetic flux density reaches 0.5 T. The solenoid, operating since 1988, was already used during the L3 experiment. As can be seen in Fig. 4.1, the main parts of the ALICE experiment are the central barrel (placed inside the solenoid) and the muon spectrometer (on the right side of the solenoid), covering the pseudorapidity ranges $|\eta| < 0.9$ and $-4.0 < \eta < -2.5$, respectively.

Starting from the innermost part of the central detector, the interaction point (IP) is surrounded by the ALICE Inner Tracking System (ITS), composed of position-sensitive silicon detectors, followed by the Time Projection Chamber (TPC), the Transition Radiation Detector (TRD) and the Time-Of-Flight Detector (TOF), all of them having a cylindrical geometry and covering the full azimuthal angle. Beyond these, several other systems are located, including the High Momentum Particle Identification Detector (HMPID), the Electromagnetic Calorimeter (EMCal) and the Photon Spectrometer (PHOS). The above mentioned detectors are used to track particles with a high precision or to identify them employing some of the common particle identification (PID) techniques.

Some detectors are located close to beam axis, at small polar angles, such as the T0, the V0, the Photon Multiplicity Detector (PMD), the Forward Multiplicity Detector (FMD) and the Zero Degree Calorimeters (ZDCs). Their importance lies in timing and trigger purposes or in their ability to estimate the orientation or centrality of nucleus-nucleus collisions. The ZDCs lie outside the L3 solenoid, at 113 m on either side of the IP [24].

Several detector systems were added during the Long Shutdown 1 of the LHC (2013-2015) to start operation at the beginning of the Run 2 (2015-2018). These include for example the Di-Jet

Calorimeter (DCal) and the Charged-Particle Veto detector (CPV), integrated with the PHOS on a common support, and the ALICE Diffractive detector (AD).

4.2 Central detectors

In this section, a more detailed description of the central-rapidity detectors, which are essential for measuring products of UPC events, will be given.

4.2.1 Inner Tracking System

The Inner Tracking System (ITS) is the detector situated closest to the beam pipe. It immediately surrounds the IP and is composed of six layers of silicon detectors exploiting three different technologies, specifically it consists of the Silicon Pixel Detector (SPD), the Silicon Drift Detector (SDD) and the Silicon Strip Detector (SSD). The main task of the ITS is to localize the primary vertex, to reconstruct the secondary vertices and to track and identify particles. It also improves results provided by the TPC and gives necessary information about the particles that traverse the dead zones of the TPC.

During the Long Shutdown 2, the ITS will be completely upgraded. The new design relies on seven layers of the ALPIDE chips, which are based on the CMOS Monolithic Active Pixel Sensors (MAPS) architecture [25]. In such a design, the sensitive volume and the readout circuitry are combined in one silicon wafer which substantially reduces the amount of material present around the beam pipe. The spatial resolution will be improved to 40 (40) μm from the current values of 240 (120) μm in the longitudinal (transverse) directions [25].

4.2.2 Time Projection Chamber

The Time Projection Chamber (TPC) is the main tracking detector in the central rapidity region. It is capable of reconstructing tracks of charged particles, measuring their momenta, identifying them and determining vertices. It covers a wide p_T range from 0.1 to 100 GeV/c and has a good ability to separate two nearby tracks. Besides the main pseudorapidity interval of $|\eta| < 0.9$ for the tracks traversing the whole TPC volume, the TPC allows to measure particles with reduced track lengths for $|\eta| < 1.5$ at reduced momentum resolution.

The device is comprised of two coaxial cylinders with inner and outer radii of ca. 85 and 250 cm respectively, and length of 500 cm. The cylinders form the electric field cage. The active volume that is filled with 90 m^3 of the optimised gas mixture of $Ne/CO_2/N_2$ in the ratio 90/10/5 is divided into two parts by the central electrode positioned halfway through the length of the cylinders. The electrode is made of a thin aluminised Mylar foil in order to reduce the amount of material that is present near the interaction point and is set to -100 kV. Other mylar strips that are wound around 18 longitudinal support rods are connected to the axial voltage dividers and provide a highly uniform electric field with an intensity of 400 V/cm.

The end plates of the apparatus are segmented into 18 inner and 18 outer trapezoidal sectors, each of them being equipped with a multi-wire proportional chamber (MWPC) with cathode pad readout. The homogeneous electric field causes the electrons produced in primary ionisation events to drift towards the end plates where they are attracted by the anode wires

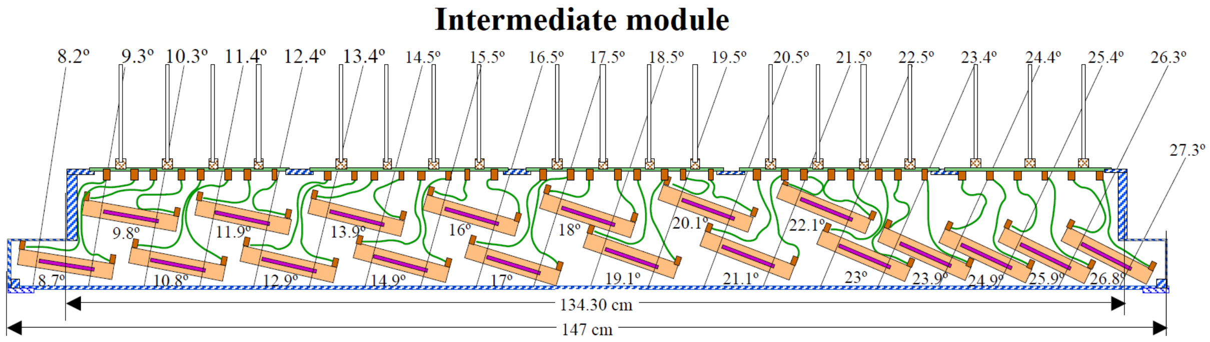

Figure 4.2: Longitudinal cross-section of the intermediate TOF modules [26]. Faces of the MRPC strips are indicated by the amber rectangles, with purple strips corresponding to active areas.

positioned in a grid above the cathode pad plane. In ALICE conditions, the maximum drift time of electrons reaches 90 μs. The movement of charged particles induces a current signal in cathode pads which then provide 2D radial coordinates with a resolution around 1 mm. Because the drift velocity is constant with a value of 2.7 cm/μs, the z coordinate is obtained from the arrival time of the primary electrons.

Normally the primary electrons produced in the sensitive volume by non-triggered events cannot reach the anode wires because the gating grid situated above the anode plane is closed. 6.5 μs after each collision, the gate is opened by the interaction trigger L1 for a time interval of 90 μs, which is equal to the maximum drift time. Since most of the positively charged ions are produced in the avalanche region in the immediate vicinity of the anode wires, the gating grid is necessary to block these ions and to prevent them from moving slowly backwards to the central electrode, inducing unwanted space-charge effects.

The whole TPC is sealed in a vessel containing insulating CO_2 atmosphere. Moreover, heat screens are installed between the TPC and the surrounding detectors such as ITS and TRD to ensure a thermal uniformity of 0.1 K inside the detector and to avoid temperature gradients which could disrupt the constant drift speed across the active volume.

4.2.3 Time-Of-Flight detector

The Time-Of-Flight (TOF) detector surrounds the TRD from outside and covers the same pseudorapidity interval $|\eta| < 0.9$ and the full azimuth. As for its role, the TOF is used to perform particle identification at intermediate momenta and to provide topological or multiplicity triggers. With an overall time resolution of 80 ps [24], it is able to distinguish between π/K and K/p with a separation of at least 3σ up to momenta of about 2.5 GeV/c for pions and kaons and 4.0 GeV/c for protons.

The TOF is mounted on the cylindrical space frame with inner (outer) radius of 370 (399) cm and a sensitive length of 741 cm. The structure is azimuthally divided into 18 sectors (supermodules), each of which is comprised of 5 gas-tight modules positioned in a row. The longitudinal cross-section of the intermediate module is depicted in Fig. 4.2. Inside these modules, the Multi-gap Resistive-Plate Chamber (MRPC) strips with dimensions of 122×13 cm^2 are installed transversely to the beam direction, forming the basic detection units of the TOF. The MRPC strips are designed with 10 gaps of 250 μm and can be operated at the atmospheric

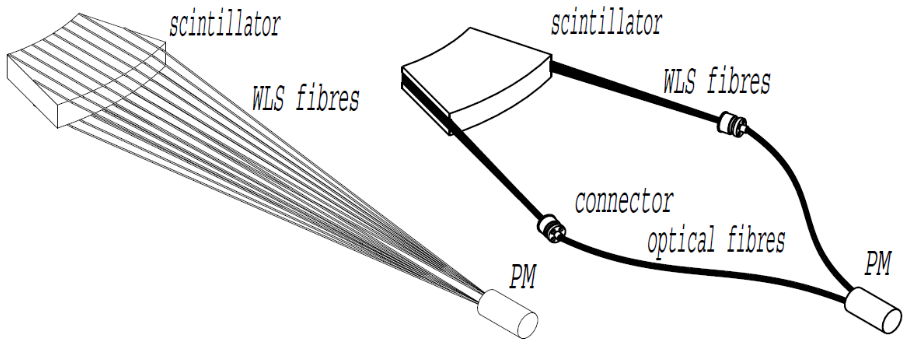

Figure 4.3: The detection elements of the V0A (left) and the V0C (right) and their connection to WLS fibres [23].

pressure. In addition, a highly uniform electric field is maintained over the sensitive volume and the presence of resistive plates prevents the formation of sparks.

A specific arrangement of the MRPC strips was chosen as evident from Fig. 4.2 to minimise the path length of the tracks deflected by the magnetic field when passing through the strips. The angle between the strips and the beam direction is 0° in the IP plane and successively increases to 45° near the end caps of the outer modules. Altogether, the TOF was designed to ensure that the occupancy of the whole system does not exceed roughly 15% at the highest anticipated multiplicities (i.e. $dN_{\mathrm{ch}}/d\eta \sim 8000$).

The operation of the TOF is closely related to the forward Cherenkov counters T0A and T0C which generate the start time for the TOF measurement. Their time resolution is $\sim 20 - 25$ ps (~ 40 ps) for Pb-Pb (pp) collisions [24]. The readout window of the TOF is equal to 500 ns [24].

In UPC triggers, the TOF is used to provide the number of triggered pads and to check up on the number of back-to-back hits with a defined opening angle.

4.3 Forward detectors

This section will focus on forward detectors that are necessary for triggering selection of UPC events. It should be first noted that for the detectors which have components covering both the forward and the backward pseudorapidity (η) sides, these are denoted by the ending -A ($\eta > 0$) and -C ($\eta < 0$) respectively.

4.3.1 V0 detector

The V0 detector is made up of two arrays of BC404 plastic scintillators located around the beam pipe at about 3.4 m (V0A) and -0.9 m (V0C) away from the IP and operating at the pseudorapidity intervals of $2.8 < \eta < 5.1$ and $-3.7 < \eta - 1.7$. Each array is segmented into four rings radially and into eight sections azimuthally. The light signals are transferred through wavelength shifting (WLS) fibres into PMTs, making use of extra clear fibres in the case of the V0C as shown in Fig. 4.3.

The V0 device is capable of estimating the centrality of the collision by recording the multiplicity in the event and thus can roughly trigger on events with specific centrality. Nonetheless, the main task of the V0 is to provide the minimum-bias (MB) trigger for the central barrel detectors in both pp and A-A collisions and to discriminate between beam-beam and unwanted beam-gas collisions. The latter is performed by controlling the arrival time of the charged particles from the primary vertex. The MB trigger is dominantly operated in an AND mode where hits in both arrays are required, however, one can also switch to an OR mode where only a hit in one direction suffices. The efficiency of the former in pp collisions averages 80%. The OR-mode MB trigger requiring hits in the V0C alone helps the muon arm in rejecting false muon events. Lastly, the luminosity measurement can be conducted employing the V0.

4.3.2 AD detector

Apart from elastic and non-diffractive collisions, a significant contribution to the total proton-proton cross section originates from single, double or central diffractive processes. Such hadronic interactions are mediated by the exchange of a colourless pomeron and can be characterised by large gaps in the rapidity distribution of products [27]. In order to enhance the capability of the ALICE apparatus to study diffractive physics, the ALICE Diffractive (AD) detector was installed during the Long Shutdown 1.

The AD is comprised of the devices ADA and ADC operating at the pseudorapidity ranges $4.8 < \eta < 6.3$ and $-7.0 < \eta < -4.9$ which are placed at a rough distance of 18 m and -20 m from the IP [27]. Both AD components are composed of two parallel layers of BC404 plastic scintillator surrounding the beam pipe, each layer being split into four cells with approximate dimensions $22 \times 20 \times 2.5$ cm^3 [27]. Again, the produced light is collected and analysed employing wavelength shifting bars, optical fibres and PMTs.

Owing to its wide pseudorapidity coverage at small angles, the AD can be considered an extension of the V0 detector. Hence, the installation of the AD enabled to investigate the rapidity gaps in diffractive processes on larger intervals and substantially improved the efficiency of the minimum-bias and the centrality triggers. Furthermore, it increased the sensitivity of ALICE to low diffractive masses and to products with lower transverse momentum [27].

Concerning the UPC triggers, the V0 and the AD are used to provide a veto on events with possible hadronic contamination. For the vector meson production at midrapidity, all four detecting components are required to detect no activity while for the forward analysis, the condition on the empty V0C is excluded because its pseudorapidity coverage largely overlaps with that of the muon spectrometer [28].

4.3.3 Zero Degree Calorimeters

The Zero Degree Calorimeter (ZDC) is a system of forward detectors which determine the centrality of an A-A collision by detecting spectator nucleons. Thanks to its position sensitivity, the ZDC can also provide an estimate of the reaction plane.

The ZDC consists of devices to detect of spectator neutrons (ZN) and protons (ZP) separately. These calorimeters are situated roughly 113 m away from the IP in both directions. Because trajectories of spectator protons are deflected by the LHC magnetic field while those of spectator neutrons are not affected, the ZNs are placed between the beam lines unlike the ZPs lying aside, as shown in Fig. 4.4. Corresponding pseudorapidity intervals are $|\eta| > 8.8$ for the

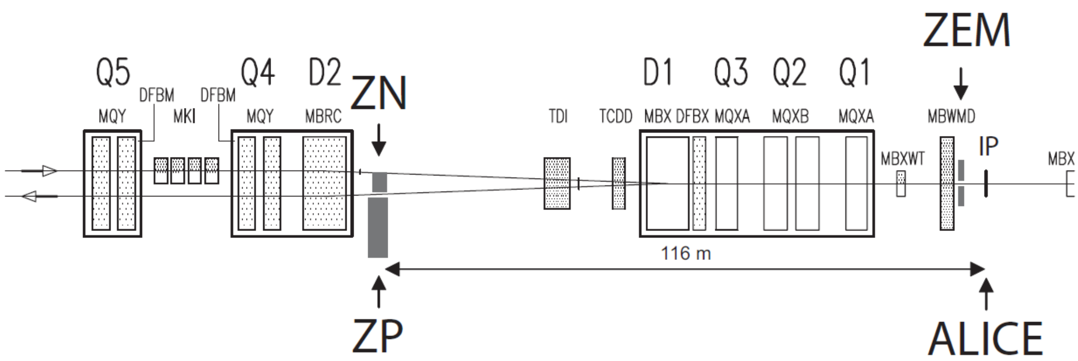

Figure 4.4: Layout of the ZDC subdetectors ZN, ZP and ZEM [23]. The distance between the hadronic calorimeters and the IP was later shortened to 113 m. Dx and Qx denote positions of the dipole and quadrupoles magnets, colliding beams are indicated by two horizontal lines.

ZNs and $6.5 < |\eta| < 7.5$ for the proton calorimeters. The last ZDC subdetector labelled ZEM consists of two components located 7 m from the IP, opposite to the muon spectrometer, and focuses on measuring electromagnetic showers in the range $4.8 < \eta < 5.7$.

Since the energy per nucleon before the collision is known, the number of spectator nucleons can be computed by measuring the total energy deposited in the forward hadronic calorimeters provided that all the spectators are detected. Each hadronic calorimeter is composed of a passive metallic absorber segmented into grooved plates. Quartz fibres which form the active medium are stretched inside the grooves. When passing through the absorbers, an incident hadron creates showers which in turn produce Cherenkov light when crossing fibres. Because the position of the ZN between the beamlines limits its transverse dimensions to ca. 7×7 cm^2, its absorber is made of a dense tungsten alloy to maximize the production of showers. The ZP, transverse dimensions of which extend up to 12×24 cm^2, makes use of brass absorbers.

The ZEM calorimeter is needed in the cases where the hadronic calorimeters cannot properly estimate the centrality of a collision. This occurs mainly in ultra-peripheral collision in which spectator nucleons are likely to remain bounded in fragments that have a similar charge-to-mass ratio to that of a heavy Pb ion. As this ratio determines the radius of curvature of the trajectory of a charged particle in a magnetic field, such fragments remain in beam pipes and thus cannot be detected. On the other hand, the ZEM, equipped with a lead absorber with quartz fibres, is designed especially to detect forward photons and the energy deposited in the ZEM decreases monotonically with decreasing centrality.

Chapter 5

Previous measurement of the incoherent J/ψ photoproduction

This chapter summarises the measurement of the incoherent J/ψ photoproduction at midrapidity $|y| < 0.9$ by the ALICE Collaboration on the data collected in 2011 during the LHC Run 1 at $\sqrt{s_{\rm NN}} = 2.76$ TeV [17]. Eq. (2.1) implies that the analysis probed the region of $x \approx 10^{-3}$. In the cited article [17], the incoherent cross section was computed together with the cross sections for the coherent and the pair photoproduction ($\gamma\gamma \rightarrow e^+e^-$) processes, results of which are also presented in this chapter.

A barrel ultra-peripheral collision (BUPC) trigger was set to trigger on events with only two tracks present in the detector, aiming to select muon or electron pairs originating either from the leptonic decay channels of charmonium or from the two-photon production. These requirements were implemented in three selections and yielded roughly 6.5×10^6 events:

- a minimum of two hits in the SPD detector,
- a number of fired pad-OR (N^{on}) in the TOF detector in the range $2 \leq N^{on} \leq 6$, with at least two of them with an azimuthal difference of $150° \leq \Delta\phi \leq 180°$,
- both the V0A and V0C detectors registered no hits.

Using a van der Meer scan, the integrated luminosity of the BUPC trigger data sample was calculated to be $L_{\rm int} = 23^{+0.7}_{-1.2}\ \mu{\rm b}^{-1}$. Furthermore, the triggered events were subjected to a set of additional cuts organised as follows:

- defining a track with loose criteria (see [17]), the number of reconstructed tracks is required to be $1 \leq N_{\rm trk} \leq 10$,
- a primary vertex is reconstructed,
- only two of the total number of tracks $N_{\rm trk}$ pass tighter quality selections (see [17]),
- at least one of the tracks selected in the previous cut has the transverse momentum $p_T \geq 1$ GeV/c (to reduce the background without affecting the signal),
- the V0 trigger veto: no signal within a time window of 25 ns around the collision time in any of the scintillating tiles in both components of the V0 (the time window is enlarged to 40 (60) ns for the V0A (V0C) in the offline analysis to increase the efficiency),

Selection	Events from 2011
Triggered events	6507692
$1 \leq N_{\text{trk}} \leq 10$	2311056
A reconstructed primary vertex	1972231
Two reconstructed tracks	436 720
At least one track with $p_T > 1$ GeV/c^2	46324
V0 offline veto	46183
dE/dx	45518
Opposite charges	31529
$2.2 < M_{\text{inv}} < 6$ GeV/c^2	4542
Coherent dielectrons	746
Incoherent dielectrons	278
Coherent dimuons	1301
Incoherent dimuons	1748

Table 5.1: Number of events remaining after the application of listed selection criteria on the LHC data from 2011 [17]. Additional cuts on coherent/incoherent events are separated by the horizontal line.

- the energy losses dE/dx of both tracks are compatible with that of electrons or muons,
- charges of the selected tracks are the same or opposite depending on the type of the analysis,
- the invariant mass of the reconstructed parent system[1] is between $2.2 < M_{\text{inv}} < 6$ GeV/c^2.

To select the dilepton candidates originating from the coherent/incoherent photoproduction, an additional criterion on the transverse momentum of the reconstructed dileptons had to be applied. The limits were set to

- $p_T < 200$ (300) MeV/c for dimuons (dielectrons) in the coherent events and
- $p_T > 200$ (300) MeV/c for dimuons (dielectrons) in the incoherent events.

The effects of all listed cuts on the number of remaining events are summed up in Tab. 5.1.

The Starlight model folded with the Monte Carlo simulations of the ALICE detectors were used to calculate the acceptance and efficiency correction $(\text{Acc} \times \varepsilon)_{\text{J}/\psi}$ for the detection of leptonic decay channels of the J/ψ mesons. The correction was computed as the ratio between the number of simulated events that meet all the criteria listed in Tab. 5.1 (including the specific cuts on the transverse momentum of dileptons) and the number of all generated events in which the J/ψ is produced in the central region of rapidity $-0.9 < y < 0.9$. The final values were found to be 2.71 (4.57)% for dielectrons (dimuons) from the coherent J/ψ and 1.8 (3.19)% for dielectrons (dimuons) produced by the incoherent J/ψ.

[1]In the context of this thesis, the parent system l^+l^- which is reconstructed from the tracks of two leptons $l^\pm$ is called a *dilepton*.

Sample	Coherent dimuons	Coherent dielectrons
N_{yield}	$291 \pm 18(\text{sta}) \pm 4(\text{sys})$	$265 \pm 40(\text{sta}) \pm 12(\text{sys})$
$N^{\text{coh}}_{\text{J}/\psi}$	$255 \pm 16(\text{sta})^{+14}_{-13}(\text{sys})$	$212 \pm 32(\text{sta})^{+14}_{-13}(\text{sys})$
$\text{d}\sigma^{\text{coh}}_{\text{J}/\psi}/\text{d}y$ [mb]	$2.27 \pm 0.14(\text{sta})^{+0.30}_{-0.20}(\text{sys})$	$3.19 \pm 0.50(\text{sta})^{+0.45}_{-0.31}(\text{sys})$
Total $\text{d}\sigma^{\text{coh}}_{\text{J}/\psi}/\text{d}y$ [mb]	$2.38^{+0.34}_{-0.24}(\text{sta}+\text{sys})$	

Table 5.2: The main experimental results obtained in the analysis of the coherent J/ψ photoproduction. See text for the definition of the variables. The values were taken from [17].

Sample	Incoherent dimuons	Incoherent dielectrons
N_{yield}	$91 \pm 15(\text{sta})^{+7}_{-5}(\text{sys})$	$61 \pm 14(\text{sta})^{+16}_{-7}(\text{sys})$
$N^{\text{incoh}}_{\text{J}/\psi}$	$81 \pm 13(\text{sta})^{+8}_{-6}(\text{sys})$	$39 \pm 9(\text{sta})^{+10}_{-5}(\text{sys})$
$\text{d}\sigma^{\text{incoh}}_{\text{J}/\psi}/\text{d}y$ [mb]	$1.03 \pm 0.17(\text{sta})^{+0.15}_{-0.12}(\text{sys})$	$0.87 \pm 0.20(\text{sta})^{+0.26}_{-0.14}(\text{sys})$
Total $\text{d}\sigma^{\text{incoh}}_{\text{J}/\psi}/\text{d}y$ [mb]	$0.98^{+0.19}_{-0.17}(\text{sta}+\text{sys})$	

Table 5.3: The main experimental results obtained in the analysis of the incoherent J/ψ photoproduction. See text for the definition of the variables. The values were taken from [17].

A comprehensive list of contributions to the systematic error of the J/ψ and $\gamma\gamma$ cross sections can be found in Table 2 in [17].

The invariant mass spectra of muon and electron pairs for both the coherent and incoherent photoproduction are depicted in Fig. 5.1. The background events coming from the processes $\gamma\gamma \to e^+e^-(\mu^+\mu^-)$ were fitted by an exponential function (with the addition of the polynomial of the 5$^{\text{th}}$ order in the case of the incoherent sample), while the signal peak was fitted by a Crystal Ball (CB) function. It is worth mentioning here that part of the underlying continuum in the incoherent sample accounts for $\pi^+\pi^-$ pairs that were misidentified due to the poor separation power of the TPC between pions and muons. The authors in [17] worked with both opposite-sign (OS) and like-sign (LS) lepton pairs to show that the LS lepton pairs occurred predominantly in the dimuon samples (see Fig. 5.1). The presence of these events should be caused mainly by the contamination from pions. Indeed, only OS pairs were used in the subsequent analysis.

Total yields of J/ψ mesons from the coherent (incoherent) samples are written in the first line of Tab. 5.2 (5.3) for muon and electron channels separately.

One of the reactions that contribute to the background is the exclusive photoproduction of ψ' that later decays into J/ψ + X. If the latter product X (not specified) is not detected in the system of detectors, the lepton pair created in the decay of the J/ψ meson can be misidentified as a decay product of the photoproduced J/ψ, even though the J/ψ itself is a product of the photoproduced ψ'. One thus defines the fraction f_D of the lepton pairs l^+l^- that were produced in decays of the coherent J/ψ mesons originating from the decay of ψ'. Analogously, the same fraction f_D can be defined for the lepton pairs coming from the J/ψ produced incoherently in the reaction $\psi' \to \text{J}/\psi + X$. The exact values of f_D for muon/electron pairs from the

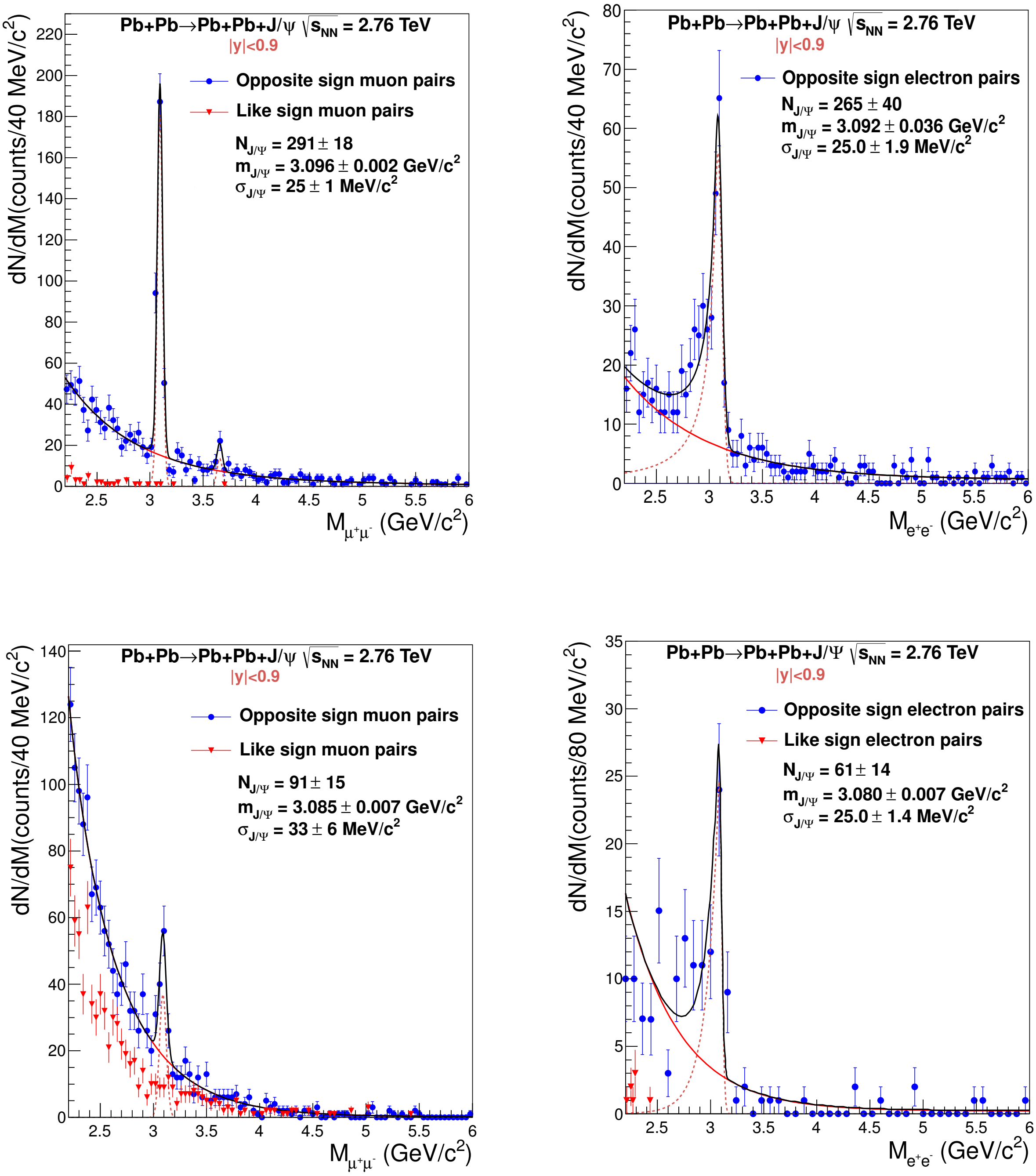

Figure 5.1: Invariant mass spectra of muon (left) and electron (right) pairs in the range $2.2 < M_{\text{inv}} < 6.0$ GeV$/c^2$ [17]. Data were collected in ultra-peripheral Pb-Pb collisions at $\sqrt{s_{\text{NN}}} = 2.76$ TeV and rapidity $|y| < 0.9$. The coherent-enriched samples are shown at the top while the incoherent-enriched samples can be found at the bottom.

coherent/incoherent J/ψ mesons are stated in [17] and, very roughly speaking, range from 5 to 15%.

Another correction that has to be taken into account is the fraction f_I of the incoherent events contaminating the coherent-enriched data sample. The calculations within the Starlight model provided the values of 0.13 (0.06) for events with electron (muon) pairs. The authors also computed the p_T distribution of dielectrons (dimuons) integrated over the invariant masses $2.2 < M_{\mathrm{inv}} < 3.2\,\mathrm{GeV}/c^2$ ($3.0 < M_{\mathrm{inv}} < 3.2\,\mathrm{GeV}/c^2$) which is shown in Fig. 5.2. In these spectra, six distinct contributions are recognised, containing dileptons from

- the coherent J/ψ photoproduction,
- the incoherent J/ψ photoproduction,
- J/ψ from the coherent decay of ψ',
- J/ψ from the incoherent decay of ψ',
- the two-photon production of continuum pairs,
- J/ψ produced in peripheral hadronic collisions.

The spectra were fitted by the sum of six functions corresponding to the above mentioned processes. The results confirmed that the computed f_I correspond (within the experimental errors) with the values provided by Starlight.

Using the newly introduced fractions f_D and f_I, a simple relation between the number of events N_{yield} calculated by fitting the peak in the invariant mass spectrum by a CB function and the desired number of coherent events $N^{\mathrm{coh}}_{J/\psi}$ can be written as

$$N^{\mathrm{coh}}_{J/\psi} = N_{\mathrm{yield}} - f_I \cdot N^{\mathrm{coh}}_{J/\psi} - f_D \cdot N^{\mathrm{coh}}_{J/\psi} \,. \tag{5.1}$$

This gives

$$N^{\mathrm{coh}}_{J/\psi} = \frac{N_{\mathrm{yield}}}{1 + f_I + f_D} \,, \tag{5.2}$$

where the analogous relation is valid for the incoherent photoproduction, except that the fraction f_D describes the incoherent J/ψ mesons from the decay of ψ' and f_I is replaced by f_C describing the coherent contamination of the incoherent-enriched sample. Again, Starlight gave the values of $f_C = 0.50$ (0.02) for dielectrons (dimuons) which were found to be in an accordance with the results from the fit of the p_T distribution.

Finally, the coherent differential cross sections can be computed employing the relation

$$\frac{\mathrm{d}\sigma^{\mathrm{coh}}_{J/\psi}}{\mathrm{d}y} = \frac{N^{\mathrm{coh}}_{J/\psi}}{(\mathrm{Acc} \times \varepsilon)_{J/\psi} \cdot BR(J/\psi \to l^+l^-) \cdot L_{\mathrm{int}} \cdot \Delta y} \,, \tag{5.3}$$

which holds also for the incoherent process when one replaces $N^{\mathrm{coh}}_{J/\psi}$ with $N^{\mathrm{incoh}}_{J/\psi}$. Here BR is the branching ratio for the J/ψ decaying into a dilepton, L_{int} is the previously-calculated integrated luminosity and Δy is the width of the rapidity interval, which is here equal to 1.8 because $-0.9 < y < 0.9$.

Tab. 5.2 (5.3) shows all the crucial results of the analysis, specifically the yield, the number of events and the cross section for the coherent (incoherent) process. Because electron and muon

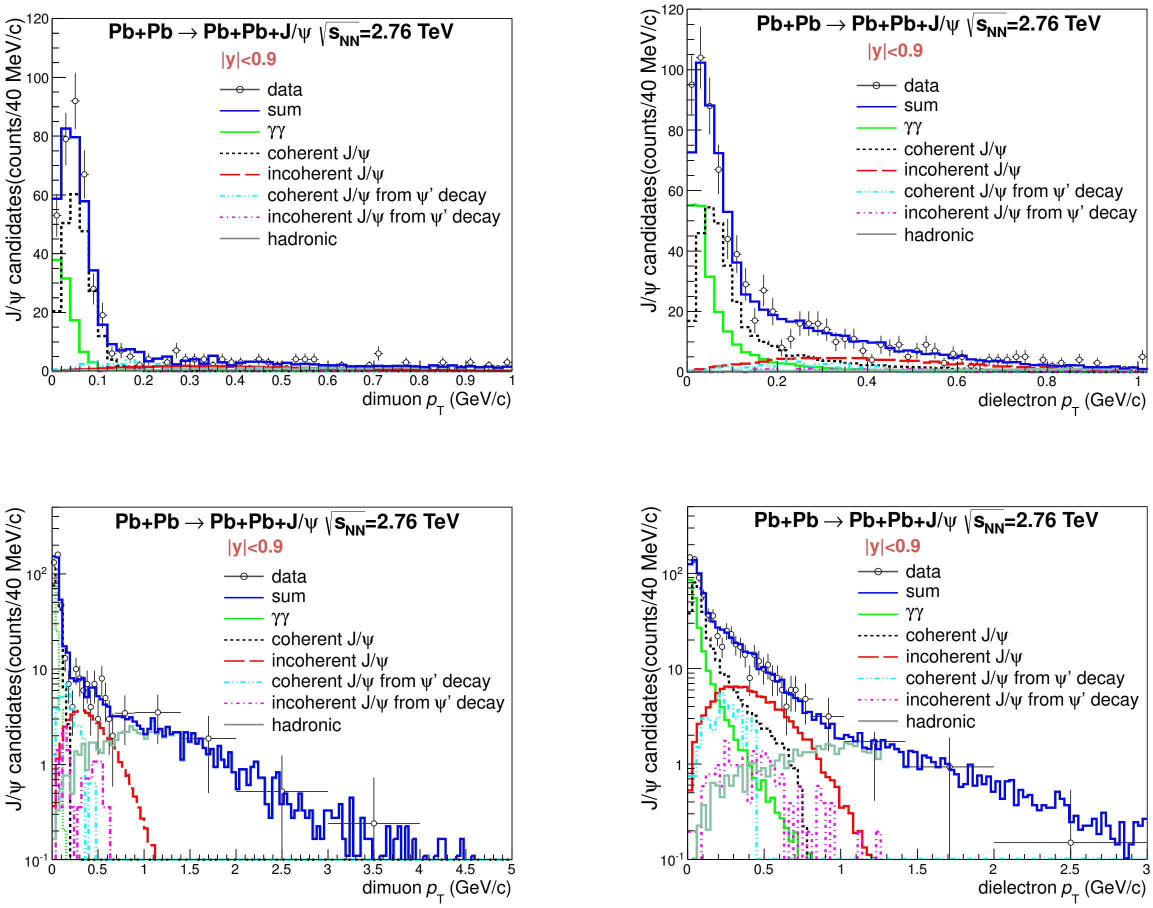

Figure 5.2: Transverse momentum distribution of muon (left) and electron (right) pairs with the invariant mass between $3.0 < M_{\mathrm{inv}} < 3.2$ GeV/c^2 and $2.2 < M_{\mathrm{inv}} < 3.2$ GeV/c^2, respectively [17]. Data were collected in ultra-peripheral Pb-Pb collisions at $\sqrt{s_{\mathrm{NN}}} = 2.76$ TeV and rapidity $|y| < 0.9$. The upper limit of the p_T interval was chosen as 1 (5) GeV/c in the top (bottom) plots. Measured values are fitted by the sum (blue) of six functions corresponding to different processes in which the lepton pair is created.

pairs are statistically independent samples, the total differential cross section of both processes can be computed as a weighted average of the electron and muons contributions. One can find these final results in the last lines of Tab. 5.2 and 5.3.

Regarding the analysis of the pair production $\gamma\gamma \to e^+e^-$, a similar relation to Eq. 5.3 holds for the pair production cross section,

$$\sigma_{\gamma\gamma} = \frac{N_{\gamma\gamma}}{(\mathrm{Acc} \times \varepsilon)_{\gamma\gamma} \cdot L_{\mathrm{int}}}, \tag{5.4}$$

where the corresponding integrated luminosity was found to be $L_{\mathrm{int}} = 21.7^{+0.7}_{-1.1}\ \mu\mathrm{b}^{-1}$ and $N_{\gamma\gamma}$ was extracted from the continuum events. In order not to mix the background dielectrons with those coming from the decay of J/ψ, the authors chose two intervals of the invariant mass M_{inv} corresponding to $2.2 < M_{\mathrm{inv}} < 2.6\ \mathrm{GeV}/c^2$ and $3.7 < M_{\mathrm{inv}} < 10\ \mathrm{GeV}/c^2$ from which the number of dielectrons $N_{\gamma\gamma}$ was extracted. Furthermore, the fourth selection on the transverse momentum of one of the tracks to be higher than 1 GeV/c was omitted.

The calculated pair production cross sections are equal to $\sigma_{\gamma\gamma} = 154 \pm 11(\mathrm{sta})^{+17}_{-11}(\mathrm{sys})\ \mu\mathrm{b}$ ($\sigma_{\gamma\gamma} = 91 \pm 10(\mathrm{sta})^{+11}_{-8}(\mathrm{sys})\ \mu\mathrm{b}$) for the former (latter) interval of invariant masses.

The main results of the article [17] are presented in Fig. 5.3. Here, the measured values of the differential coherent (incoherent) cross sections are compared with predictions of six (three) different models. The models implement various models of the photonuclear interaction, which constitutes the main source of differences between their predictions. While the coherent cross section is in a good accordance with the AB-EPS09 model that incorporates the nuclear gluon shadowing, none of the models is able to predict correctly the measured value of the incoherent cross section. The Starlight model does not give correct values of the coherent and incoherent cross sections individually, nevertheless, it provides an incoherent-to-coherent ratio of 0.41 that accords with the results.

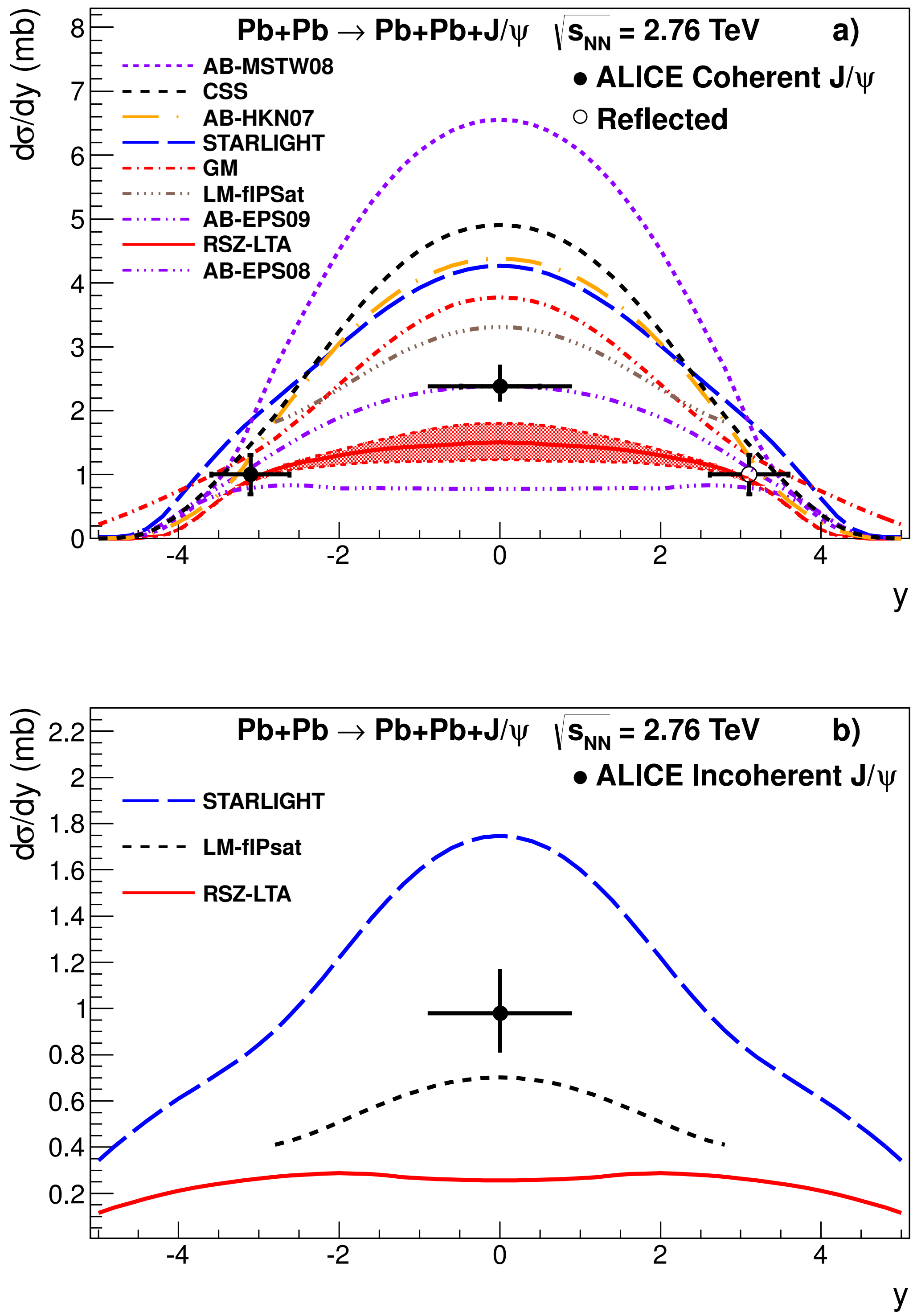

Figure 5.3: Measured differential cross section of the coherent (top) and incoherent (bottom) J/ψ photoproduction in ultra-peripheral Pb-Pb collisions at $\sqrt{s_{\mathrm{NN}}} = 2.76$ TeV at $|y| < 0.9$ [17]. Both results are compared with predictions of different models. For the specification of each model see [17].

Chapter 6

Data analysis

The analysis of the incoherent J/ψ photoproduction in the midrapidity region in ultra-peripheral collisions at the LHC is presented in this chapter. The analysed data sets were collected in lead-lead collisions at a centre-of-mass energy $\sqrt{s_{\mathrm{NN}}} = 5.02$ TeV during the periods LHC18q and LHC18r. These periods differ in the reversed polarity of the L3 solenoid magnet [29].

6.1 Data flow at ALICE

The Data Preparation Group (DPG) of ALICE is the research team responsible for the reconstruction and calibration of the data measured by ALICE and has to provide Quality Assurance of the collected events. Initially, the data coming from the ALICE detectors are stored in the raw format. When the calibration is performed and the tracks and vertices are reconstructed, the data are stored within the Event Summary Data (ESD) objects. ESD files can be in general used as an input to analysis, but working with them might be inefficient due to their large size since they also contain information which are not needed by most of the analyses. After filtering, a lighter format called the Analysis Object Data (AOD) is created, which should be used for a subsequent physics analysis.

The distribution, storage and analysis of the data is carried out on the Worldwide LHC Computing Grid (simply abbreviated as Grid). Using the LEGO train system, one can run over the AOD files on the Grid and select only events with fired UPC triggers. In this way, the so called nano-AODs are created. Due to the extremely low multiplicites of the UPC events, the UPC nano-AODs are very compact. UPC nano-AODs were used as an input to the analysis presented in this thesis.

6.2 Data samples

For the corresponding periods LHC18q [30] and LHC18r [31], the DPG published lists of the so-called good runs, which fulfil qualitative requirements regarding the operation parameters and the stability of the basic set of ALICE subsystems needed for the analyses. The analysis was performed on the data from the first reconstruction stage: LHC18q_pass1 and LHC18r_pass1.

The list of good runs passing the CCUP31 trigger (see Section 6.3) in LHC18q includes 123 runs, specifically

295585, 295586, 295588, 295589, 295610, 295611, 295612, 295615, 295666, 295667, 295668, 295673, 295675, 295676, 295712, 295714, 295717, 295718, 295719, 295721, 295723, 295725, 295754, 295755, 295758, 295759, 295762, 295763, 295786, 295788, 295791, 295816, 295818, 295819, 295822, 295825, 295826, 295829, 295831, 295853, 295854, 295855, 295856, 295859, 295860, 295861, 295909, 295910, 295913, 295936, 295937, 295941, 295942, 296016, 296060, 296062, 296063, 296065, 296066, 296123, 296132, 296133, 296134, 296135, 296142, 296143, 296191, 296192, 296194, 296195, 296196, 296197, 296198, 296240, 296241, 296242, 296243, 296244, 296246, 296247, 296269, 296270, 296273, 296279, 296280, 296303, 296304, 296309, 296312, 296377, 296378, 296379, 296380, 296381, 296383, 296414, 296415, 296419, 296420, 296423, 296424, 296433, 296472, 296509, 296510, 296511, 296512, 296516, 296547, 296548, 296549, 296550, 296551, 296552, 296553, 296594, 296615, 296616, 296618, 296619, 296621, 296622, 296623.

For the period LHC18r, the analogous runlist contains 96 runs, namely

296690, 296691, 296693, 296694, 296749, 296750, 296781, 296784, 296785, 296786, 296787, 296790, 296793, 296794, 296799, 296835, 296836, 296838, 296839, 296848, 296849, 296850, 296851, 296852, 296890, 296894, 296899, 296900, 296903, 296930, 296931, 296932, 296934, 296935, 296938, 296941, 296966, 297029, 297031, 297035, 297085, 297117, 297118, 297119, 297123, 297124, 297128, 297129, 297132, 297133, 297193, 297194, 297195, 297196, 297218, 297219, 297221, 297222, 297278, 297310, 297311, 297317, 297332, 297333, 297335, 297336, 297363, 297366, 297367, 297372, 297379, 297380, 297405, 297406, 297413, 297414, 297415, 297441, 297442, 297446, 297450, 297451, 297452, 297479, 297481, 297483, 297512, 297537, 297540, 297541, 297542, 297544, 297558, 297588, 297590, 297595.

6.3 UPC triggers in 2018

The analysed events were triggered by the central barrel UPC trigger class CCUP31. For the run numbers up to 295880, the trigger CCUP31-B-NOPF-CENTNOTRD = !0VBA !0VBC !0UBA !0UBC 0STG 0OMU was used, where NOPF denotes that it was operated with no past-future protection, B stands for beam-beam collision and

- !0VBA (!0VBC) = no signal in the V0A (V0C) during the beam-beam time window,
- !0UBA (!0UBC) = no signal in the ADA (ADC) during the beam-beam time window,
- 0STG = SPD topological trigger demanding at least two back-to-back tracklets[1] with a predefined opening angle and
- 0OMU = between two and six hits in the TOF detector with at least two of them having an opening angle larger than 150°.

Starting from the run 295881 the events were triggered by CCUP31-B-SPD2-CENTNOTRD, where the SPD2 past-future protection on the six previous bunch crossings was introduced.

[1]Tracklets are short track segments made of two hits, each in a different layer of the SPD detector.

6.4 Selection of events

In this analysis, the J/ψ particles are reconstructed from the decays into lepton pairs (e^+e^- or $\mu^+\mu^-$) produced in the central rapidity region. In order to extract the events with relevant lepton pairs, a set of selections had to be applied on the data sample consisting of the nano-AODs for the runs listed in Section 6.2. The cuts were ordered as follows:

- An AOD event is non-empty.
- The event consists of just two good central tracks according to both the TPC and SPD detectors. A good TPC track is required to satisfy `TestFilterBit(1«5)`, while that of SPD has to meet the criterion `HasPointOnITSLayer(0) && HasPointOnITSLayer(1)`. The definition of the former function can be found in [32], whereas the latter selection requires the tracks to have clusters in both layers of the SPD detector.
- The event was triggered by CCUP31-B-NOPF-CENTNOTRD if the run number is below 295881 or was triggered by CCUP31-B-SPD2-CENTNOTRD in the opposite case.
- The invariant mass of the reconstructed dilepton is $m \in (2.2, 4.5)$ GeV/c^2.
- AD offline veto (both the ADA and ADC detectors have to be empty).
- V0 offline veto (both the V0A and V0C detectors have to be empty).
- Rapidity of the dilepton is in the central range, i.e. $|y| < 0.8$ (to exclude potential border effects).
- Pseudorapidity η of both tracks is $|\eta| < 0.8$.
- Tracks have opposite charges.
- Muon pairs can be additionally selected by applying the criterion

$$\sigma^2_{\mu,\,1} + \sigma^2_{\mu,\,2} < \sigma^2_{e,\,1} + \sigma^2_{e,\,2}\,,$$

  where $\sigma_{\mu,\,i}$ is the distance, measured in standard deviations, between the energy loss due to ionisation expectated for a muon and the measured energy loss of the i-th track. The definition of $\sigma_{e,\,i}$ is analogous.

Table 6.1 summarises the number of events passing each of the selections. The next-to-last row shows the effect of filtering out the electron-positron pairs. One can see that in both periods the muon pairs account for ca. 65% of all selected events. Alternatively in the last row, the J/ψ candidates with invariant mass in the immediate vicinity of the J/ψ mass $M_{J/\psi} = 3.096$ GeV/c^2 were selected from both electrons and muons. These events will be used in Section 6.7 when plotting the transverse momentum distribution. For the fit of the invariant mass distributions presented in Section 6.6, the last cut was not relevant.

Selection	LHC18q	LHC18r
Two good central tracks	981184	1521030
CCUP31 trigger	835170	1441881
Dilepton invariant mass $m \in (2.2, 4.5)$ GeV/c^2	20749	34009
ADA offline veto	20718	33830
ADC offline veto	20700	33690
V0A offline veto	17896	28962
V0C offline veto	16106	26153
Dilepton rapidity $\|y\| < 0.8$	15859	25744
Pseudorapidity of both tracks $\|\eta\| < 0.8$	12769	20509
Opposite charges	11582	18562
$\mu^+\mu^-$ pairs only	7525	11953
Dilepton invariant mass $m \in (3.0, 3.2)$ GeV/c^2	2952	4552

Table 6.1: Number of remaining events in the periods LHC18q and LHC18r passing the applied criteria.

6.5 Luminosity calculation

In order to evaluate the amount of accessed data, the calculations of integrated luminosity L_{int} were performed for both analysed periods. In Fig. 6.1 and 6.2, one can find the comparison of analysed and recorded integrated luminosities. The reference values (recorded luminosities) for the corresponding periods are stored in so-called trending files [33], which contain the number of events N_{rec} fired by a given trigger in each run. The analysed luminosity in a run is obtained by simply scaling the recorded values of L_{int} by the ratio of the number of analysed events N_{ana} fired by a given trigger to N_{rec}.

The total recorded luminosity of the CCUP31 trigger in 2018 (with the past-future protection starting from the run 295881 as described in Section 6.3) was found to be 245.634 μb^{-1}, while the analysed value amounts to approximately 97% of the former. One of the contributions to the 3% loss are computational errors during the analysis of large data samples on GRID.

6.6 Invariant mass distribution

First of all, the invariant mass distributions of the coherently produced J/ψ mesons were created, so that the results could be compared to the official existing analysis of the same data set examining the coherent photoproduction [32]. The main steps of the analyses for the measurement of the coherent and the incoherent cross sections are similar. They differ in the fact that in the first case the signal is concentrated at lower transverse momenta than in the later, as highlighted in Section 2.1.1. To obtain clean signals one applies a selection on the transverse momentum. In the following, the coherent-enriched sample, obtained by selecting events with $p_T < 0.11$ GeV/c, is studied and a comparison is made with [32]. Then, the events with $p_T > 0.2$ GeV/c and $p_T > 0.3$ GeV/c are studied.

It was found that the results presented in this work agree with the corresponding results

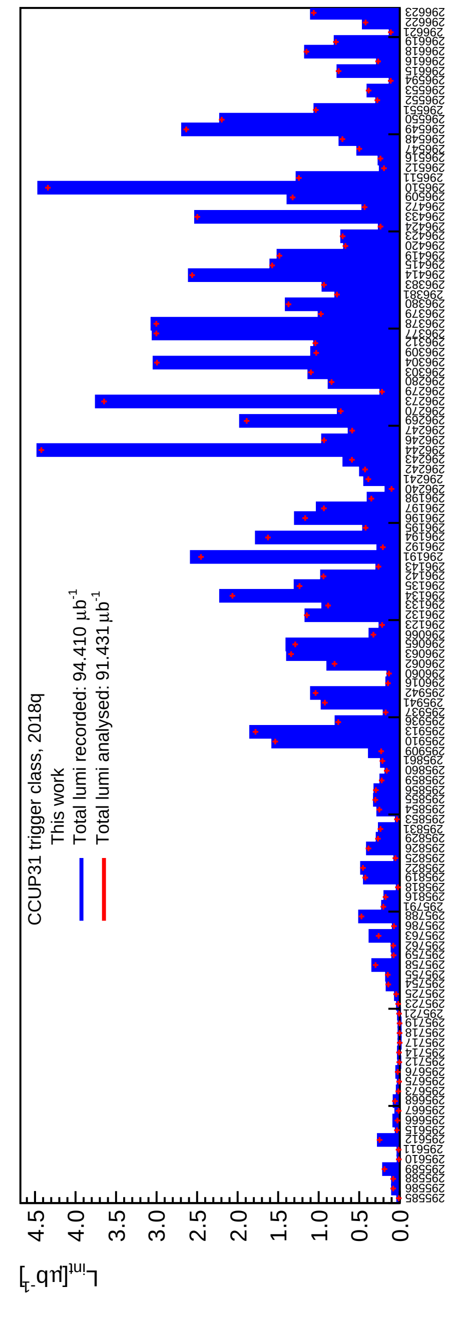

Figure 6.1: Integrated luminosity L_{int} of the CCUP31 trigger class per run in the period LHC18q. Blue columns indicate recorded values while red crosses correspond to values analysed in this study.

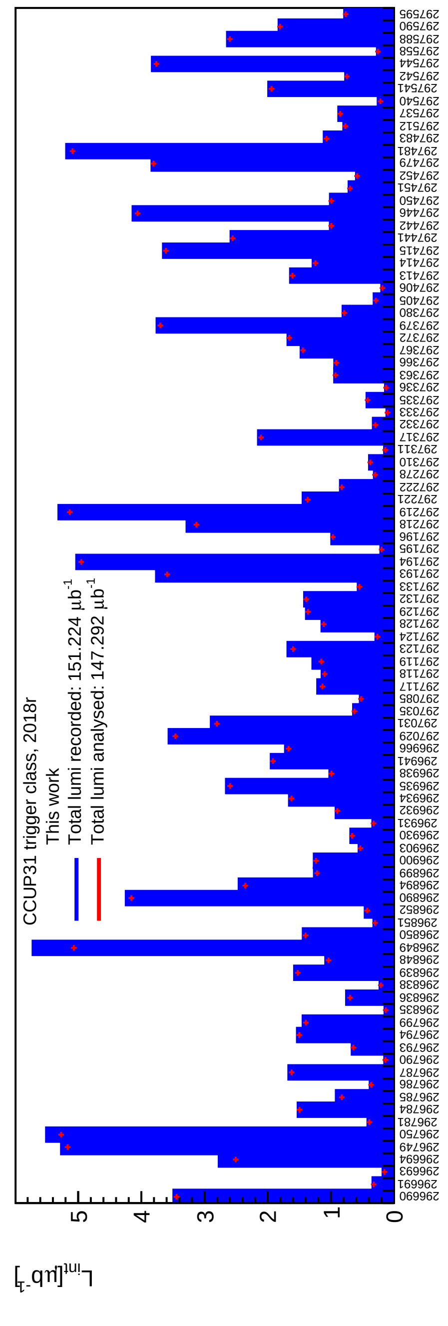

Figure 6.2: Integrated luminosity L_{int} of the CCUP31 trigger class per run in the period LHC18r. Blue columns indicate recorded values while red crosses correspond to values analysed in this study.

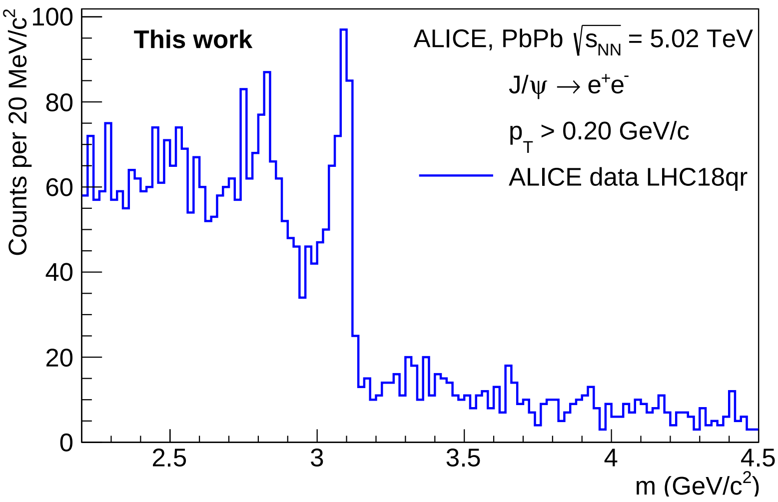

Figure 6.3: The invariant mass spectrum of e^+e^- pairs with the transverse momentum of the e^+e^- pair $p_T > 0.2$ GeV/c. The data from both periods are merged.

from the mentioned analysis [34], which validates the procedure and the results presented in the following.

The signal peak of the J/ψ meson was fitted by a Crystal Ball (CB) function with parameters $M_{\mathrm{J}/\psi}$, σ, n, α and a normalisation factor $N_{\mathrm{J}/\psi}$, while the background signal in the invariant mass distribution was described by a pure exponential function $N_{\mathrm{bg}} \exp(\lambda m)$ with an exponential slope parameter $\lambda < 0$ GeV^{-1} c^2. In addition, a second CB function was added in the cases where the contribution from the $\psi(2S)$ meson with the mass $M_{\psi(2S)} = 3.686$ GeV/c^2 was clearly non-negligible. However, values of the σ, n and α parameters were chosen to be common for both signal peaks and the mass $M_{\psi(2S)}$ was fixed to the above stated value of 3.686 GeV/c^2, leaving only one additional free parameter, the normalisation $N_{\psi(2S)}$.

In Fig. 6.5a and 6.5b (6.6a and 6.6b), one can find fitted invariant mass distributions of muon (electron) pairs with the cut on the transverse momentum of the dilepton $p_T < 0.11$ GeV/c. This selection aims for the extraction of the coherently photoproduced mesons which were analysed in [32]. Following the same strategy as in [32], the α and n parameters were fixed to the values of 1.795 and 16.452, respectively, when fitting the invariant mass spectrum of dimuons. One can easily notice the lower resolution when working with electron-positron pairs, represented by the tails of the CB function falling less rapidly in the region of lower invariant masses. From now on, only muon pairs are considered in the analysis of the incoherent photoproduction as the lower resolution and a limited amount of data made it difficult to obtain reasonable results from the fitting of the invariant mass spectra of e^+e^-. As an example, the spectrum of e^+e^- masses for the period LHC18r with the cut $p_T > 0.2$ GeV/c is depicted in Fig. 6.3.

Two cuts on the transverse momentum of a dimuon were applied to extract the vector mesons produced mostly via incoherent photoproduction. In Fig. 6.7a and 6.7b (6.8a and 6.8b), the fitted spectra of invariant masses with the cuts $p_T > 0.2$ GeV/c ($p_T > 0.3$ GeV/c) are shown. Events with higher transverse momenta are characterised by larger multiplicities in the region of low invariant masses ($m \lesssim 3.0$ GeV/c^2) which manifests itself by larger values of the λ parameter ($\simeq -2$). The parameters quoted without errors were fixed during the fitting procedure. One can see that in all cases, the number of produced $\psi(2S)$ particles is close to zero and therefore it is arguable whether to include the $\psi(2S)$ CB function in the model as the $\psi(2S)$ peaks are of a similar order as statistical fluctuations.

Now, one can try to compare the numbers $N_{\mathrm{J}/\psi}$ in Fig. 6.7a and 6.7b, corresponding to the number of J/ψ particles with $p_T > 0.2$ GeV/c that decayed into muon pairs, with the analogous quantity N_{yield} in Tab. 5.3, extracted from the Run 1 data. One sees that the sum of events from the periods LHC18q and LHC18r is roughly eight times higher than the previous value. This means that a reduction of the statistical error by almost a factor of three can be achieved and it will be possible to perform more systematic studies to reduce the systematic uncertainty.

Eventually, the rapidity dependence of the invariant mass spectrum was inspected by additionally cutting the previously analysed regions of the transverse momentum into two regions of rapidity with roughly the same number of J/ψ mesons. The motivation lies in the fact that the regions of Bjorken x sampled in different intervals of rapidity y are different as indicated by Eq. 2.1. Thus, the study of the rapidity dependence may offer new experimental constraints to the energy dependence of the incoherent production at small Bjorken x.

The limit was taken as $|y| = 0.25$, so the regions correspond to $0.80 > |y| > 0.25$ and $|y| < 0.25$, respectively. The resulting plots can be found in Fig. 6.9 to 6.12. In all plots, the parameter n was fixed to the value of 2.5, other parameters were fitted to experimental data.

6.7 Transverse momentum distribution

The transverse momentum distribution of the analysed sample is shown in Fig. 6.4. The signal is composed of both muon and electron pairs, merged for the both periods. Note that only the J/ψ candidates with the invariant mass $m \in (3.0, 3.2)$ GeV/c^2 were plotted. As displayed in Fig. 5.2 and in [32], the transverse momentum distribution can be fitted using several components (apart from the coherent and incoherent J/ψ photoproduction, also the possibility of the production of J/ψ from the decay of $\psi(2S)$ or $\gamma\gamma$ interactions have to be included), which will be one of the goals of the next step of this study.

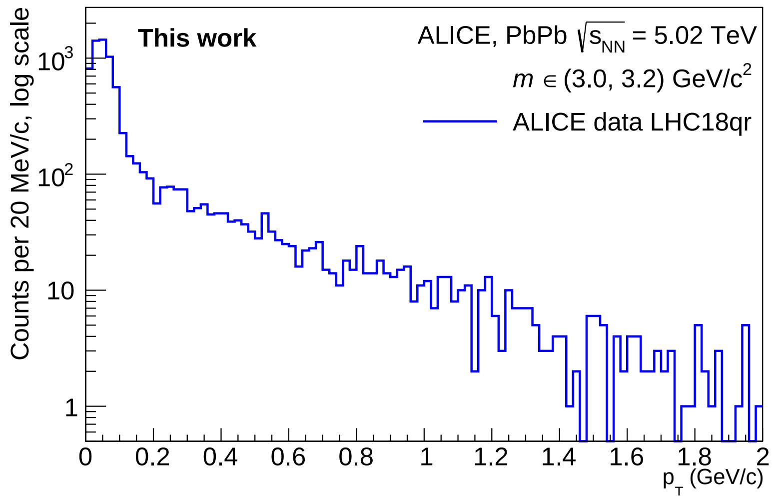

Figure 6.4: The transverse momentum spectrum of events with the invariant mass of the reconstructed dilepton system $m \in (3.0, 3.2)$ GeV$/c$. The data from both periods are merged.

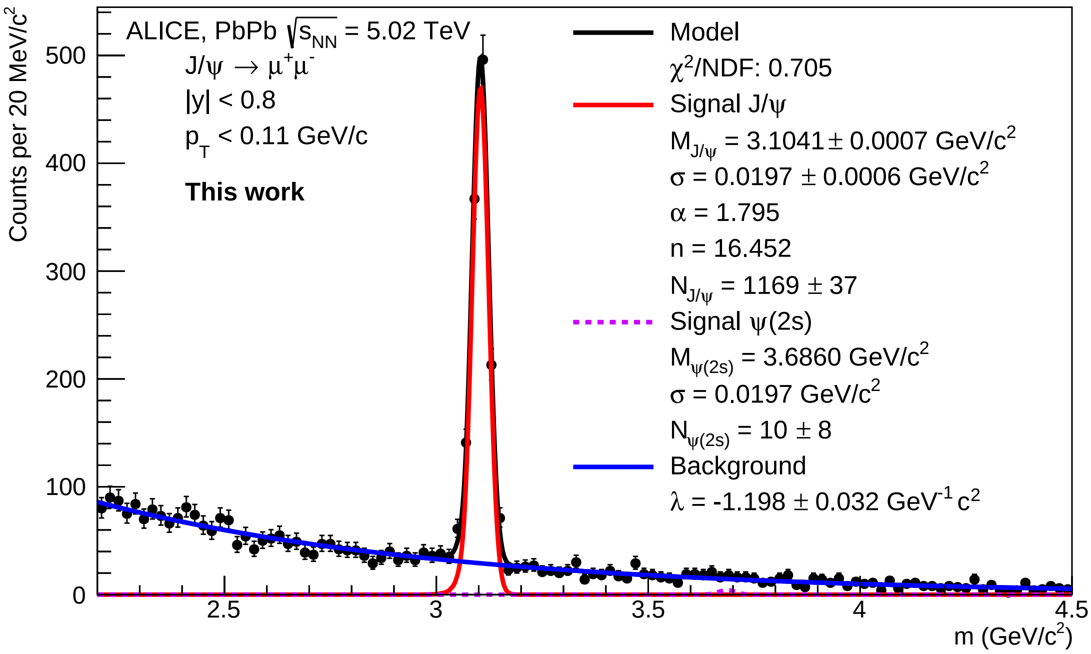

(a) LHC18q

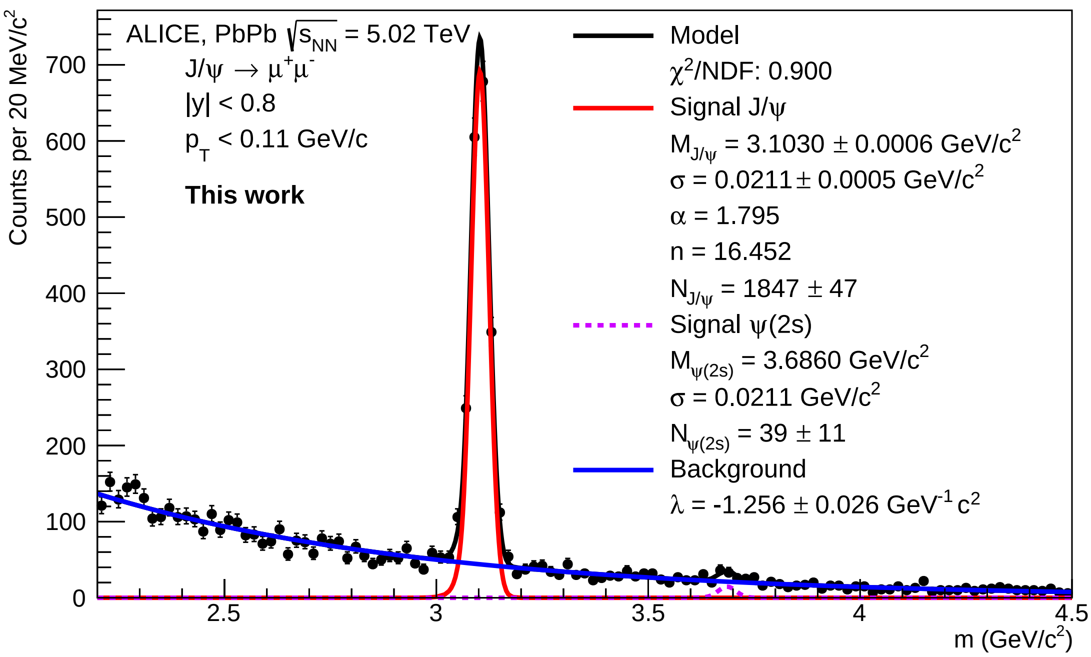

(b) LHC18r

Figure 6.5: Fitted invariant mass spectra of selected $\mu^+\mu^-$ pairs with the cut $p_T < 0.11$ GeV$/c$ for the corresponding periods.

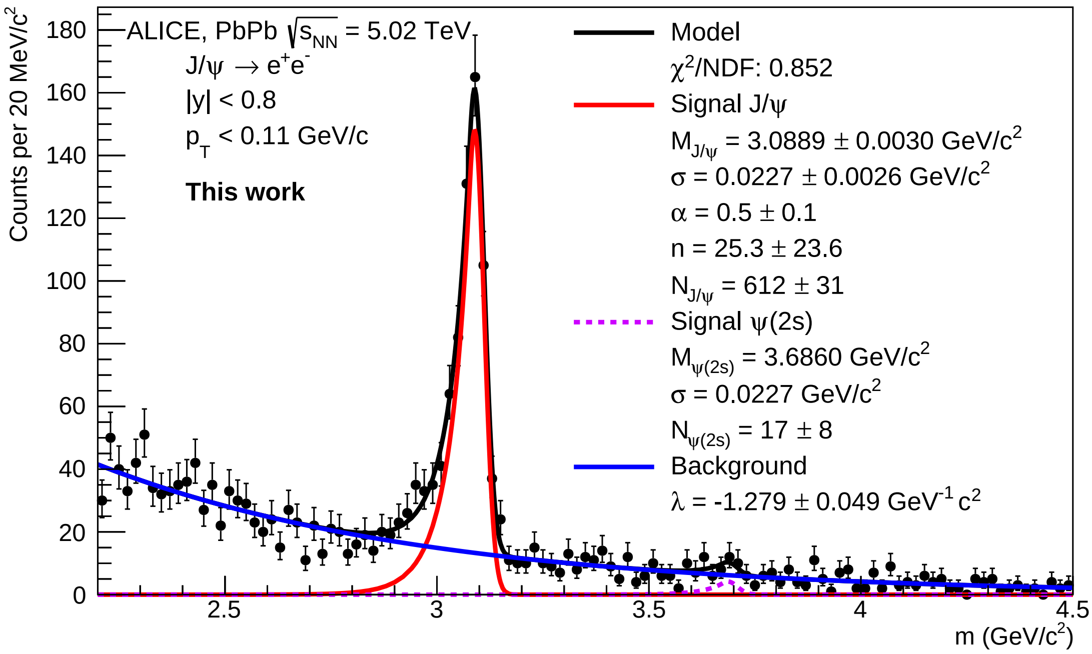

(a) LHC18q

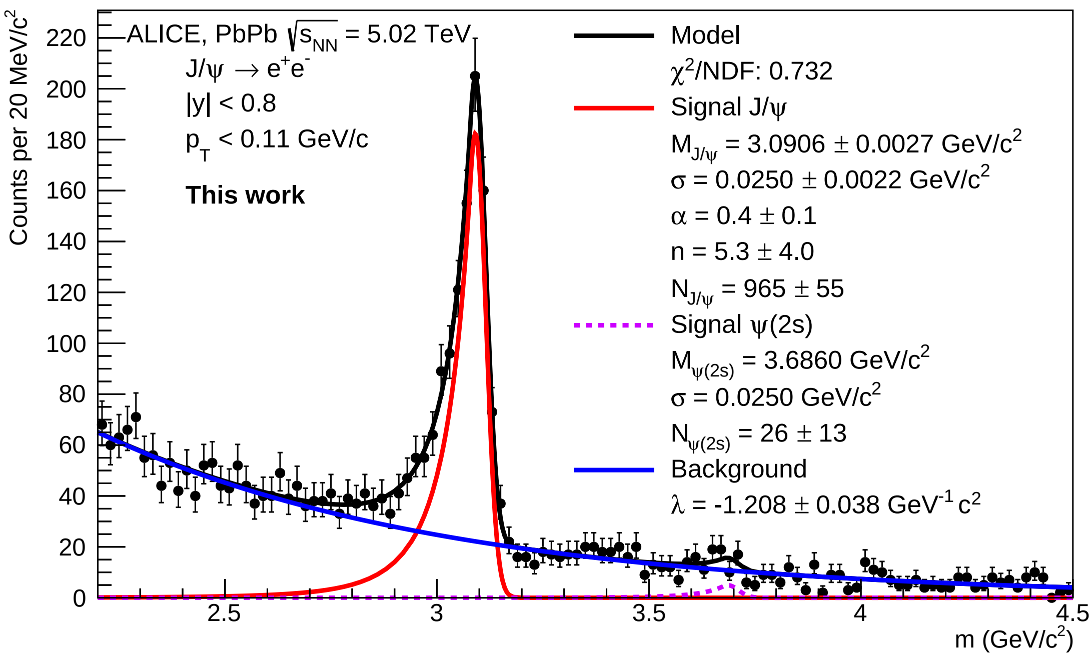

(b) LHC18r

Figure 6.6: Fitted invariant mass spectra of selected e^+e^- pairs with the cut $p_T < 0.11$ GeV$/c$ for the corresponding periods.

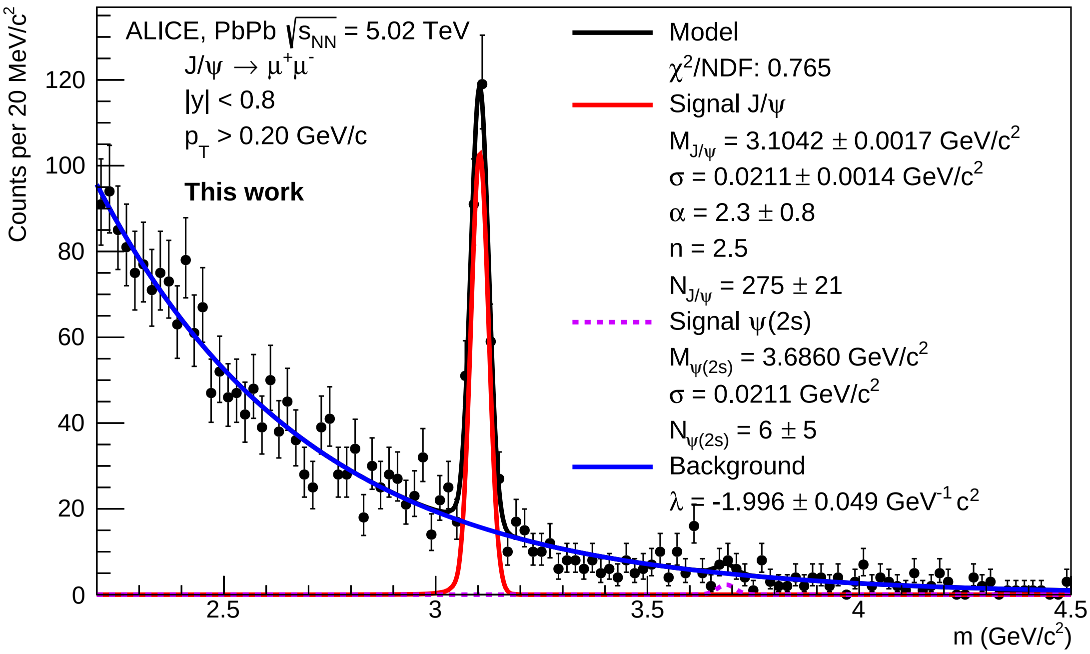

(a) LHC18q

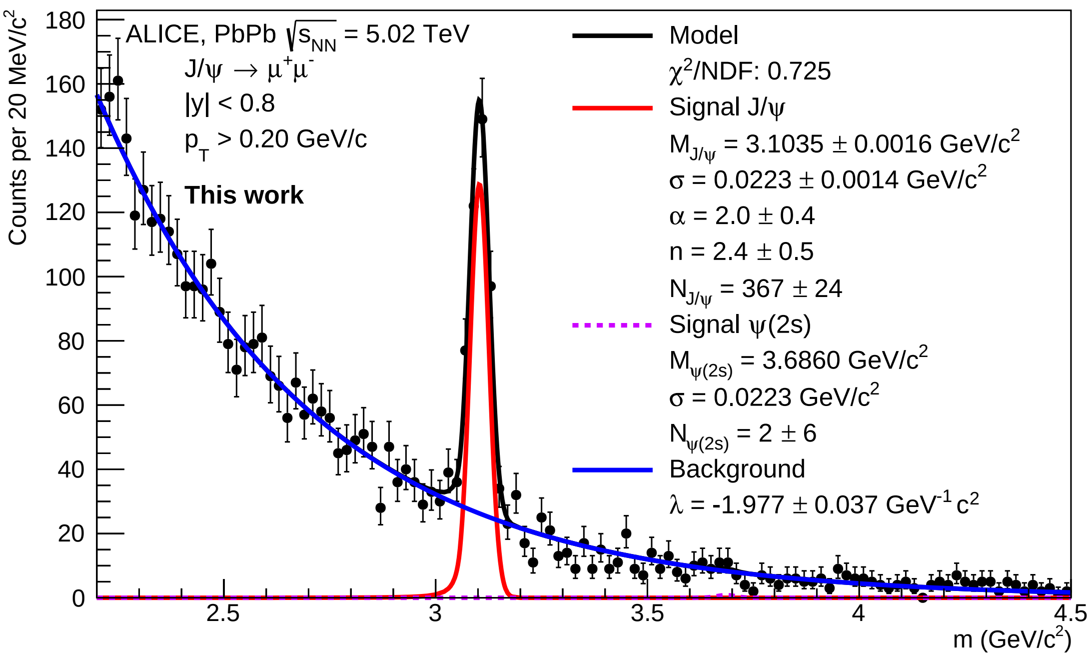

(b) LHC18r

Figure 6.7: Fitted invariant mass spectra of selected $\mu^+\mu^-$ pairs with the cut $p_T > 0.2$ GeV$/c$ for the corresponding periods.

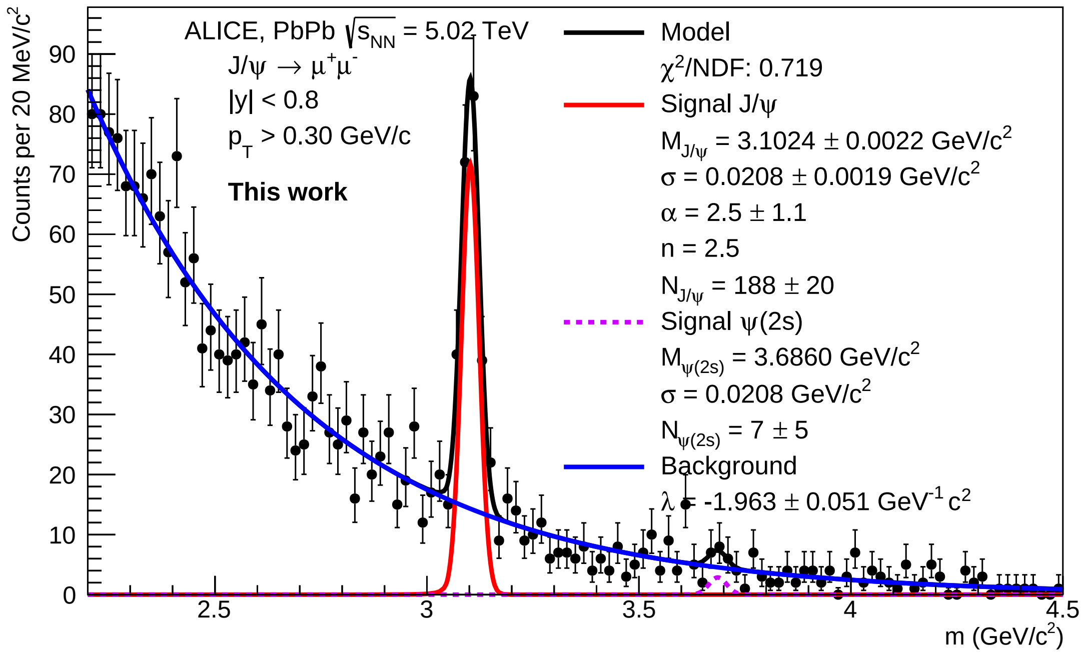

(a) LHC18q

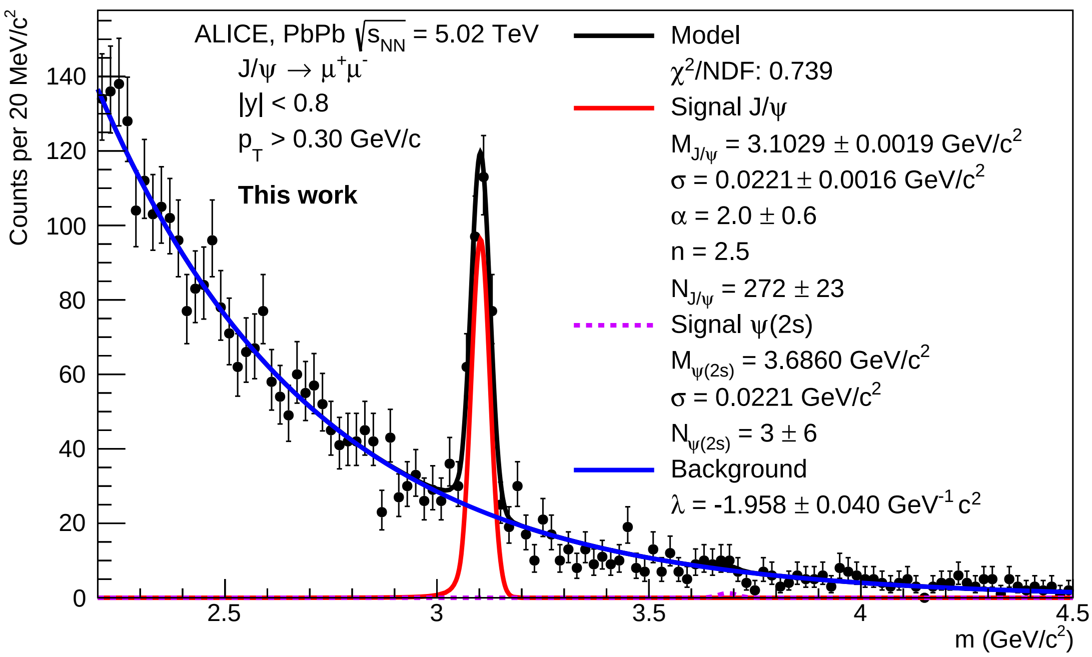

(b) LHC18r

Figure 6.8: Fitted invariant mass spectra of selected $\mu^+\mu^-$ pairs with the cut $p_T > 0.3$ GeV/c for the corresponding periods.

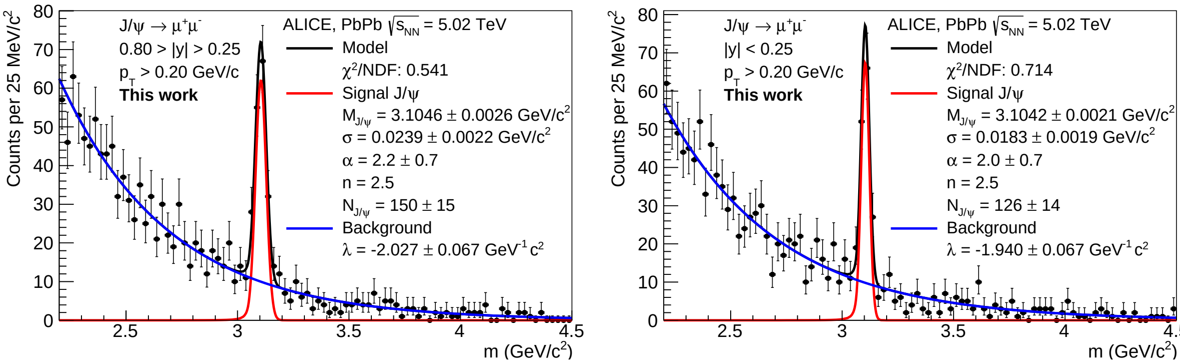

Figure 6.9: The invariant mass spectra of $\mu^+\mu^-$ pairs with the reconstructed dimuon's $p_T > 0.2$ GeV$/c$, $0.80 > |y| > 0.25$ (left) and $|y| < 0.25$ (right). Data are from the period LHC18q.

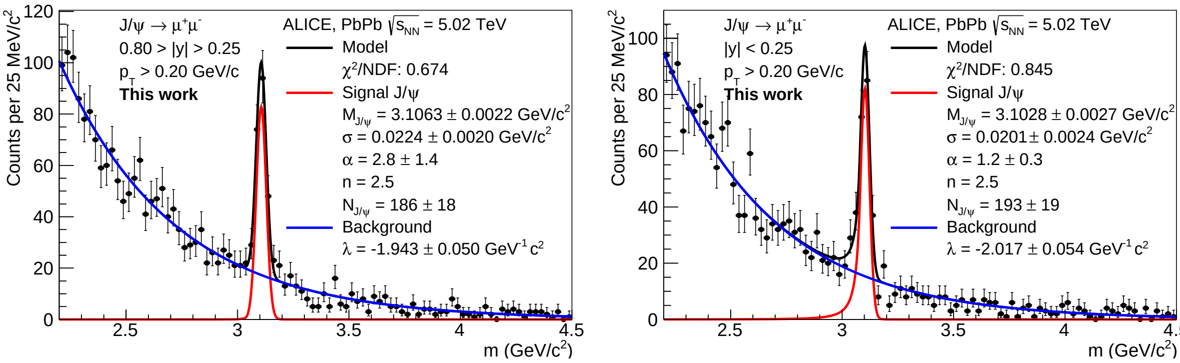

Figure 6.10: The invariant mass spectra of $\mu^+\mu^-$ pairs with the reconstructed dimuon's $p_T > 0.2$ GeV$/c$, $0.80 > |y| > 0.25$ (left) and $|y| < 0.25$ (right). Data are from the period LHC18r.

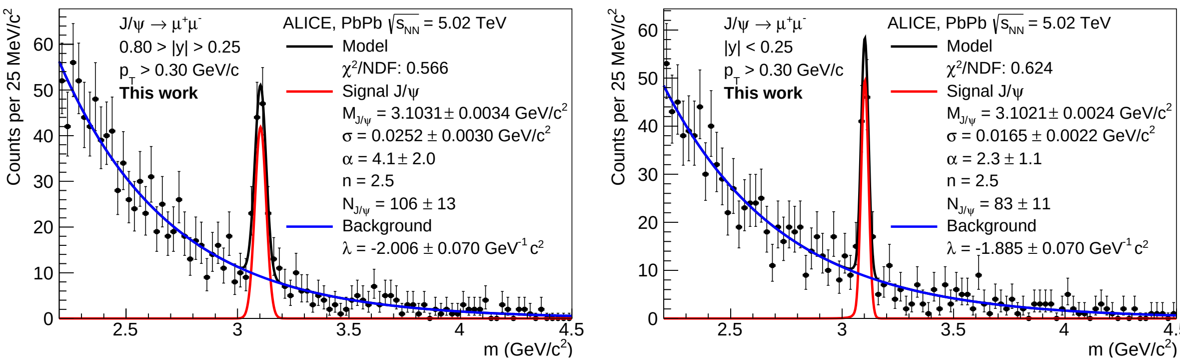

Figure 6.11: The invariant mass spectra of $\mu^+\mu^-$ pairs with the reconstructed dimuon's $p_T > 0.3$ GeV$/c$, $0.80 > |y| > 0.25$ (left) and $|y| < 0.25$ (right). Data are from the period LHC18q.

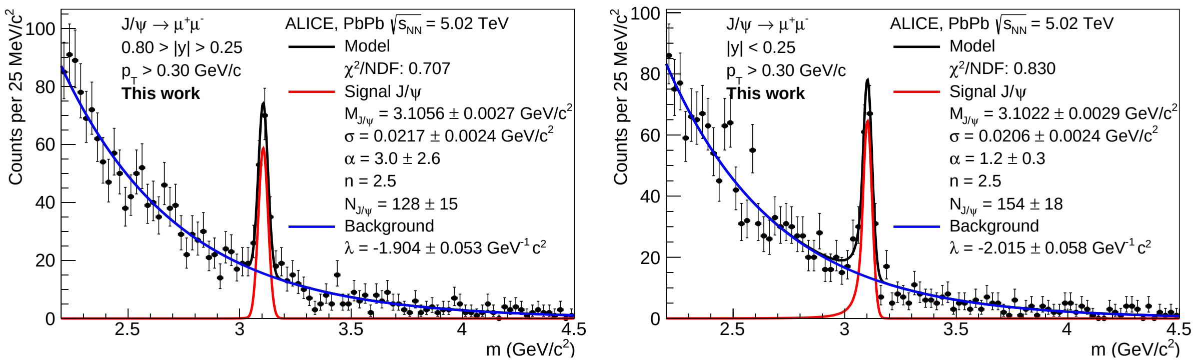

Figure 6.12: The invariant mass spectra of $\mu^+\mu^-$ pairs with the reconstructed dimuon's $p_T > 0.3$ GeV/c, $0.80 > |y| > 0.25$ (left) and $|y| < 0.25$ (right). Data are from the period LHC18r.

Conclusion

The structure of hadrons described in terms of the parton distribution functions (PDFs) was introduced in Chapter 1. The PDFs show significant evolution with the energy of the probe. It should be reminded here that in the low Bjorken-x region hadrons appear to be composed of a high number of gluons and beyond the saturation scale Q_s, the recombination processes are expected to occur, manifesting itself by the phenomenon of gluon saturation.

In Chapter 2, ultra-peripheral collisions were examined, which play an important role in probing the hadron structure. In particular, the photoproduction of the J/ψ vector meson was introduced. The electromagnetic part of the process is nowadays satisfactorily described by the approach of equivalent photons, which was briefly introduced in Section 2.2, while several models exist to address the latter part of the interaction including the strong force. Among these, the colour dipole model occupies an important place. On the other hand, from the models employing the leading order pQCD, one can directly show that the cross section of the coherent photoproduction is proportional to the square of the gluon PDF. This clearly demonstrates the connection between UPCs and the structure of hadrons.

An energy-dependent hot-spot was introduced in Chapter 3. It was shown that measured coherent and incoherent cross sections of the J/ψ photoproduction are in a satisfactory agreement with the predictions of the model describing the transverse structure of nucleons as a sum of Gaussian-shaped hot spots, the number of which grows with the increasing energy of the collision. Moreover, when applied to the dissociative photoproduction of J/ψ off the proton, the model seems to have a potential to predict effects of gluon saturation.

The ALICE detectors dedicated to the measurement of UPCs were described in detail in Chapter 4. The previous measurement of both the coherent and incoherent midrapidity photoproduction of J/ψ in heavy-ion collisions at $\sqrt{s_{\mathrm{NN}}} = 2.76$ TeV by ALICE was presented afterwards in Chapter 5. Results of this study will constitute an important reference point for the future results of the incoherent J/ψ midrapidity photoproduction at higher energies.

Finally, my contribution to the analysis of the midrapidity ($|y| < 0.8$) J/ψ photoproduction in heavy-ion UPCs at $\sqrt{s_{\mathrm{NN}}} = 5.02$ TeV from the periods LHC18q and LHC18r of the LHC Run 2 was presented in Chapter 6. On the analysed data samples, selection criteria aiming to select dimuons and dielectrons coming from both the coherently and incoherently photoproduced J/ψ were applied. A comparison with the existing analysis of the coherent-enriched sample was performed to show that both results are compatible. In addition to the calculation of the integrated luminosity of the analysed samples for the utilized UPC triggers, the invariant mass distributions of the muon and electron pairs were plotted and fitted by the sum of an exponential and a CB functions for various p_T and central rapidity intervals.

The presented results constitute the primary steps in the analysis of the incoherent J/ψ photoproduction. My intent is to continue working on the contribution to the analysis of the 2018 UPC data samples, aim of which is to calculate the cross section of the incoherent photoproduction. One of the next steps will be to fit the measured p_T distributions using the functions given by MC simulations and corresponding to different processes in which the lepton pairs are created.

Bibliography

[1] Mark A. Thomson. *Handout 6: Deep Inelastic Scattering*. https://www.hep.phy.cam.ac.uk/~thomson/partIIIparticles/handouts/Handout_6_2011.pdf. Accessed on 3rd Nov 2019. 2011.

[2] G.D. Coughlan and J.E. Dodd. *The Ideas of Particle Physics: An Introduction for Scientists*. Cambridge University Press, 1991. ISBN: 9780521386777.

[3] Jerome I. Friedman. "Deep inelastic scattering: Comparisons with the quark model". In: *Rev. Mod. Phys.* 63 (1991), pp. 615–629. DOI: 10.1103/RevModPhys.63.615.

[4] F.D. Aaron et al. "Combined Measurement and QCD Analysis of the Inclusive e+- p Scattering Cross Sections at HERA". In: *JHEP* 01 (2010), p. 109. DOI: 10.1007/JHEP01(2010)109. arXiv: 0911.0884 [hep-ex].

[5] C. Adloff et al. "Measurement and QCD analysis of neutral and charged current cross-sections at HERA". In: *Eur. Phys. J. C* 30 (2003), pp. 1–32. DOI: 10.1140/epjc/s2003-01257-6. arXiv: hep-ex/0304003.

[6] B.R. Martin and G. Shaw. *Particle Physics*. Manchester Physics Series. Wiley, 2008. ISBN: 9780470721537.

[7] Francois Gelis et al. "The Color Glass Condensate". In: *Ann. Rev. Nucl. Part. Sci.* 60 (2010), pp. 463–489. DOI: 10.1146/annurev.nucl.010909.083629. arXiv: 1002.0333 [hep-ph].

[8] Heikki Mäntysaari. "Balitsky-Kovchegov equation". In: (2011).

[9] The DOE/NSF Nuclear Science Advisory Committee. *The Frontiers of Nuclear Science, A Long Range Plan*. 2008. arXiv: 0809.3137 [nucl-ex].

[10] J. G. Contreras and J. D. Tapia Takaki. "Ultra-peripheral heavy-ion collisions at the LHC". In: *Int. J. Mod. Phys.* A30 (2015), p. 1542012. DOI: 10.1142/S0217751X15420129.

[11] A.J. Baltz. "The Physics of Ultraperipheral Collisions at the LHC". In: *Phys. Rept.* 458 (2008). Ed. by G. Baur et al., pp. 1–171. DOI: 10.1016/j.physrep.2007.12.001. arXiv: 0706.3356 [nucl-ex].

[12] J. Cepila, J. G. Contreras and J. D. Tapia Takaki. "Energy dependence of dissociative J/ψ photoproduction as a signature of gluon saturation at the LHC". In: *Phys. Lett.* B766 (2017), pp. 186–191. DOI: 10.1016/j.physletb.2016.12.063. arXiv: 1608.07559 [hep-ph].

[13] Heikki Mäntysaari and Björn Schenke. "Evidence of strong proton shape fluctuations from incoherent diffraction". In: *Phys. Rev. Lett.* 117.5 (2016), p. 052301. DOI: 10.1103/PhysRevLett.117.052301. arXiv: 1603.04349 [hep-ph].

[14] E.L. Kryshen. "Photoproduction of heavy vector mesons in ultra-peripheral Pb-Pb collisions". In: *Nucl. Phys. A* 967 (2017). Ed. by Ulrich Heinz, Olga Evdokimov and Peter Jacobs, pp. 273–276. DOI: 10.1016/j.nuclphysa.2017.05.083. arXiv: 1705.06872 [nucl-ex].

[15] J.G. Contreras. "Gluon shadowing at small x from coherent J/ψ photoproduction data at energies available at the CERN Large Hadron Collider". In: *Phys. Rev. C* 96.1 (2017), p. 015203. DOI: 10.1103/PhysRevC.96.015203. arXiv: 1610.03350 [nucl-ex].

[16] V. Guzey, E. Kryshen and M. Zhalov. "Coherent photoproduction of vector mesons in ultraperipheral heavy ion collisions: Update for run 2 at the CERN Large Hadron Collider". In: *Phys. Rev. C* 93 (5 2016), p. 055206. DOI: 10.1103/PhysRevC.93.055206. URL: https://link.aps.org/doi/10.1103/PhysRevC.93.055206.

[17] E. Abbas et al. "Charmonium and e^+e^- pair photoproduction at mid-rapidity in ultra-peripheral Pb-Pb collisions at $\sqrt{s_{\mathrm{NN}}}$=2.76 TeV". In: *Eur. Phys. J.* C73.11 (2013), p. 2617. DOI: 10.1140/epjc/s10052-013-2617-1. arXiv: 1305.1467 [nucl-ex].

[18] Jan Cepila, Jesus Guillermo Contreras and Michal Krelina. "Coherent and incoherent J/ψ photonuclear production in an energy-dependent hot-spot model". In: *Phys. Rev.* C97.2 (2018), p. 024901. DOI: 10.1103/PhysRevC.97.024901. arXiv: 1711.01855 [hep-ph].

[19] Gerhard Baur et al. "Coherent gamma gamma and gamma-A interactions in very peripheral collisions at relativistic ion colliders". In: *Phys. Rept.* 364 (2002), pp. 359–450. DOI: 10.1016/S0370-1573(01)00101-6. arXiv: hep-ph/0112211.

[20] Carlos A. Bertulani, Spencer R. Klein and Joakim Nystrand. "Physics of ultra-peripheral nuclear collisions". In: *Ann. Rev. Nucl. Part. Sci.* 55 (2005), pp. 271–310. DOI: 10.1146/annurev.nucl.55.090704.151526. arXiv: nucl-ex/0502005.

[21] Lyndon Evans and Philip Bryant. "LHC Machine". In: *JINST* 3 (2008), S08001. DOI: 10.1088/1748-0221/3/08/S08001.

[22] Steve Myers. "The greatest lepton collider". In: *CERN Courier* 59.5 (Aug. 2019), pp. 39–43.

[23] K. Aamodt et al. "The ALICE experiment at the CERN LHC". In: *JINST* 3 (2008), S08002. DOI: 10.1088/1748-0221/3/08/S08002.

[24] Betty B. Abelev et al. "Performance of the ALICE Experiment at the CERN LHC". In: *Int. J. Mod. Phys.* A29 (2014), p. 1430044. DOI: 10.1142/S0217751X14300440. arXiv: 1402.4476 [nucl-ex].

[25] D. Andreou. "The upgrade of the ALICE Inner Tracking System". In: *JINST* 14.05 (2019), p. C05004. DOI: 10.1088/1748-0221/14/05/C05004. arXiv: 1904.13237 [physics.ins-det].

[26] *ALICE Time-Of-Flight system (TOF): Technical Design Report*. Technical Design Report ALICE. Geneva: CERN, 2000. URL: https://cds.cern.ch/record/430132.

[27] G. Corral. "Diffractive physics with ALICE at the LHC: The control of quantum collisions". In: *Journal of Physics: Conference Series* 624 (June 2015). DOI: 10.1088/1742-6596/624/1/012008.

[28] Christopher Daniel Anson. "Photoproduction of vector mesons in ultra-peripheral Pb-Pb interactions with ALICE". In: *CERN Proc.* 1 (2018). Ed. by David d'Enterria, Albert de Roeck and Michelangelo Mangano, p. 131. DOI: 10.23727/CERN-Proceedings-2018-001.131.

[29] ALICE DPG. *Reconstructed Run-2 data taking periods: Pb-Pb*. https://twiki.cern.ch/twiki/bin/view/ALICE/AliDPGReconstructedDataTakingPeriodsPbPb. Accessed: 2020-06-15.

[30] ALICE DPG. *Lists of good runs for LHC18q*. https://twiki.cern.ch/twiki/bin/view/ALICE/AliDPGRunList18q. Accessed: 2020-06-15.

[31] ALICE DPG. *Lists of good runs for LHC18r*. https://twiki.cern.ch/twiki/bin/view/ALICE/AliDPGRunList18r. Accessed: 2020-06-15.

[32] Roman Lavička. *Analysis note: t-Dependence of coherent photo-production of J/Psi in Pb-Pb ultra-peripheral collisions*. https://alice-notes.web.cern.ch/system/files/notes/analysis/1083/2020-07-02-AN_2018UPCjpsiont.pdf. Accessed: 2020-07-09.

[33] ALICE UPC group. *Ultra-Peripheral Collisions at ALICE*. https://twiki.cern.ch/twiki/bin/viewauth/ALICE/UltraPeripheralCollisions. Accessed: 2020-07-09.

[34] Roman Lavička. *Private communication*. 2020.